



1 **Impact of ambient conditions on the Si isotope fractionation in marine pore**
2 **fluids during early diagenesis**

3
4 Sonja Geilert¹, Patricia Grasse¹, Kristin Doering^{1,2}, Klaus Wallmann¹, Claudia Ehlert³, Florian Scholz¹,
5 Martin Frank¹, Mark Schmidt¹, Christian Hensen¹

6
7 ¹GEOMAR Helmholtz Centre for Ocean Research Kiel, Wischhofstr. 1-3, 24148 Kiel, Germany

8 ²Department of Oceanography, Dalhousie University, Halifax, Canada

9 ³Marine Isotope Geochemistry, ICBM, University of Oldenburg, Germany

10

11 ABSTRACT

12

13 Benthic fluxes of dissolved silica (Si) from sediments into the water column are driven by the
14 dissolution of biogenic silica (bSiO₂) and terrigenous Si minerals and modulated by the precipitation
15 of authigenic Si phases. Each of these processes has a specific effect on the isotopic composition of
16 silica dissolved in sediment pore waters such that the determination of pore water δ³⁰Si values can
17 help to decipher the complex Si cycle in surface sediments. In this study, the δ³⁰Si signatures of pore
18 fluids and bSiO₂ in the Guaymas Basin (Gulf of California) were analyzed, which is characterized by
19 high bSiO₂ accumulation and hydrothermal activity. The δ³⁰Si signatures were investigated in the
20 deep basin, in the vicinity of a hydrothermal vent field, and at an anoxic site located within the
21 pronounced oxygen minimum zone (OMZ). The pore fluid δ³⁰Si_{pf} signatures differ significantly
22 depending on the ambient conditions. Within the basin, δ³⁰Si_{pf} is essentially uniform averaging
23 +1.2±0.1‰ (1SD). Pore fluid δ³⁰Si_{pf} values from within the OMZ are significantly lower (0.0±0.5‰,
24 1SD), while pore fluids close to the hydrothermal vent field are higher (+2.0±0.2‰, 1SD).

25 Reactive transport modelling results show that the δ³⁰Si_{pf} is mainly controlled by silica dissolution
26 (bSiO₂ and terrigenous phases) and Si precipitation (authigenic aluminosilicates). Precipitation
27 processes cause a shift to high pore fluid δ³⁰Si_{pf} signatures, most pronounced at the hydrothermal
28 site. Within the OMZ however, additional dissolution of isotopically depleted Si minerals (e.g. clays)
29 facilitated by high mass accumulation rates of terrigenous material (MAR_{terr}) is required to promote
30 the low δ³⁰Si_{pf} signatures while precipitation of authigenic aluminosilicates seems to be hampered by
31 high water/rock ratios. Guaymas OMZ δ³⁰Si_{pf} values are markedly different from those of the
32 Peruvian OMZ, the only other marine setting where Si isotopes have been investigated to constrain
33 early diagenetic processes. These differences highlight the fact that δ³⁰Si_{pf} signals in OMZs worldwide
34 are not alike and each setting can result in a range of δ³⁰Si_{pf} values as a function of the environmental



35 conditions. We conclude that the benthic silica cycle is more complex than previously thought and
36 that additional Si isotope studies are needed to decipher the controls on Si turnover in marine
37 sediment and the role of sediments in the marine silica cycle.

38

39 KEYWORDS: Si isotopes, reverse weathering, hydrothermal system, oxygen minimum zone,
40 environmental conditions

41

42 1. INTRODUCTION

43

44 Silicon (Si) is one of the key macronutrients in the ocean mainly utilized by siliceous organisms such
45 as diatoms, radiolarians or sponges (see recent review by Sutton et al., 2018). The marine Si cycle is
46 closely linked to the carbon (C) cycle by marine siliceous organisms, which transport C to the
47 sediment and thus exert a strong control on C export from the atmosphere impacting present and
48 past climate (e.g. Lewin, 1961; Tréguer and Pondaven, 2000; Tréguer and De La Rocha, 2013; and
49 recent reviews by Frings et al., 2016 and Sutton et al., 2018). Studies of Si isotopes ($\delta^{30}\text{Si}$) have
50 revealed complex uptake and dissolution processes of siliceous organisms, which have a dominant
51 control on the $\delta^{30}\text{Si}$ distribution in ocean waters (e.g. de la Rocha et al., 1997; Varela, 2004; Cardinal
52 et al., 2005; Beucher et al., 2008; Fripiat et al., 2011; Ehlert et al., 2012; Grasse et al., 2013; Sutton et
53 al., 2013; de Souza et al., 2014, 2015). Diatoms constitute the largest part of the Si cycling fluxes in
54 the ocean (Ragueneau et al., 2000) and discriminate between its isotopes during Si uptake, whereby
55 the light isotopes are preferentially incorporated into the diatom frustules (e.g. de la Rocha et al.,
56 1997). Si isotope fractionation during silica uptake is dependent on e.g. the diatom species, the
57 availability of Fe, and the degree of silica utilization. Fractionation factors between -0.5 and -2.1‰
58 have been derived from regional water mass mixing and laboratory studies (de la Rocha et al., 1997;
59 Varela, 2004; Cardinal et al., 2005; Beucher et al., 2008; Sutton et al., 2013; Meyerink et al., 2017).

60 After a planktonic bloom whereupon the nutrients are exhausted, biogenic silica (bSiO_2 , mainly
61 diatoms) sinks through the ocean, partially dissolves and accumulates on the seafloor, where its
62 preservation and recycling is controlled by dissolution and Si re-precipitation processes. The
63 dissolution of bSiO_2 mainly controls the accumulation of silicic acid (Si(OH)_4) in pore fluids, although
64 the in-situ concentration remains below the equilibrium concentration of dissolved bSiO_2 , which has
65 been explained by simultaneous formation of authigenic silicates (e.g. McManus et al., 1995; Van
66 Cappellen and Qiu, 1997a, b; Rickert et al., 2002). This process is termed reverse weathering given
67 that the authigenic precipitates are rich in seawater-derived cations, like Na, K or Mg (Mackenzie et
68 al., 1981; Michalopoulos and Aller, 1995). Experimental studies of bSiO_2 dissolution kinetics revealed
69 a dependence of the bSiO_2 reactivity on sediment depth as well as the ratio between terrigenous



70 material and bSiO₂ (Michalopoulos and Aller, 1995; Van Cappellen and Qiu, 1997a, b; Dixit et al.,
71 2001; Rickert et al., 2002). Marine weathering of terrigenous material (primary silicates like feldspars
72 and secondary silicates like clays), was found to release cations such as aluminum (Al) or iron (Fe),
73 which reduce the solubility and dissolution rate of bSiO₂ and induce aluminosilicate precipitation
74 (Michalopoulos and Aller, 1995; Van Cappellen and Qiu, 1997a, b; Michalopoulos et al., 2000; Dixit et
75 al., 2001; Rickert et al., 2002; Loucaides et al., 2010). The accumulation of Si in pore fluids and the Si
76 reflux into bottom waters are controlled by three interdependent processes, namely: opal
77 dissolution, dissolution of terrigenous solids, precipitation of authigenic minerals.

78 Early silica diagenesis has been shown to fractionate Si isotopes as a function of the crystallization
79 state, seawater Si concentration, sedimentation rate, and terrigenous mineral content (Tatzel et al.,
80 2015; Geilert et al., 2016). Since the light ²⁸Si isotope is more reactive compared to the heavier
81 isotopes (²⁹Si, ³⁰Si), processes such as reverse weathering, adsorption, and direct silica precipitation
82 from saturated solutions show low δ³⁰Si values in the reaction product and high δ³⁰Si values in its
83 substrate (i. e. fluids) (e.g. Georg et al., 2006a, 2009; Delstanche et al., 2009; Opfergelt et al., 2013;
84 Geilert et al., 2014; Roerdink et al., 2015; Ehlert et al., 2016). The few modelling and experimental
85 studies, addressing Si isotope fractionation during formation of secondary phases, report isotope
86 fractionation factors between -1.6 and -2‰ (Ziegler et al., 2005; Méheut et al., 2007; Dupuis et al.,
87 2015; Ehlert et al., 2016).

88 The δ³⁰Si data for marine pore waters from the Peruvian margin upwelling region, which is
89 characterized by very high diatom productivity and bSiO₂-rich sediments (Abrantes et al., 2007;
90 Bruland et al., 2005), agree with these findings and clearly indicate Si isotope fractionation as a
91 consequence of authigenic aluminosilicate precipitation accompanied by a Si isotope fractionation
92 factor of -2.0‰ (Ehlert et al., 2016). Also pore fluids from the Greenland margin and Labrador Sea
93 reflect early diagenetic reactions detected by pore fluid δ³⁰Si values (between +0.76 and +2.08‰)
94 and the δ³⁰Si values were interpreted as the product of reverse weathering reactions (Ng et al.,
95 2020). In this study, the Guaymas Basin in the Gulf of California was chosen as study area, as it is
96 characterized by a relatively high diatom productivity and sediments that are predominantly
97 composed of diatomaceous muds (up to 50% diatoms; Kastner and Siever, 1983). Moreover, the
98 Guaymas Basin in the Gulf of California is influenced by hydrothermal activity (e.g. Von Damm, 1990).
99 These bSiO₂-rich sediments are thus ideal for dedicated studies of early diagenesis under the
100 influence of different thermal and redox conditions. We investigated the processes controlling Si
101 isotope fractionation during early diagenesis based on pore fluid and bSiO₂ data from three
102 fundamentally different environmental settings within the Guaymas Basin including the deep basin, a
103 hydrothermal site, and a site within the Oxygen Minimum Zone (OMZ) on the slope of the Guaymas
104 Basin (Fig. 1). In addition, the Si isotope composition of the water column, bottom waters, and



105 hydrothermal fluids was determined. A numerical transport-reaction model was applied to the OMZ
106 setting to constrain marine weathering processes and to compare the results to the Peruvian margin.
107 The aim of this study was to constrain the factors controlling Si isotope fractionation during early
108 diagenesis and to identify processes influencing bSiO_2 dissolution and authigenic silicate
109 precipitation.

110

111 2. GEOLOGICAL SETTING, SAMPLING, AND METHODS

112

113 2.1 Geological setting

114

115 The Guaymas Basin in the Gulf of California is a currently opening continental rifting environment
116 with two graben systems (northern and southern trough), which are offset by a transform fault and
117 reaches spreading rates of up to 6 cm yr^{-1} (Calvert, 1966). High biological productivity and
118 terrigenous matter input result in high sediment accumulation rates and have produced thick
119 sequences of organic-rich sediments (DeMaster, 1981; Curray and Moore, 1982). Siliceous sediments
120 at the Guaymas Slope show fine laminations within the OMZ (dissolved oxygen $<10 \mu\text{M}$ at ca. 500 –
121 900 m water depth; Campbell and Gieskes, 1984) due to the absence of burrowing organisms
122 (Calvert, 1964). The Guaymas Basin is characterized by vigorous hydrothermal activity represented
123 by Black Smoker type vents discovered in both the northern and southern troughs (Berndt et al.,
124 2016; Von Damm et al., 1985). Hydrothermal plumes spread horizontally and mix with deep basin
125 water up to 300 m above the seafloor resulting in a fraction of hydrothermal fluids of $\sim 0.1\%$ in the
126 deep waters of the Guaymas Basin (Campbell and Gieskes, 1984). Hydrothermal sills and dikes
127 intruding into the sediments were found to accelerate early diagenetic reactions (due to the released
128 heat) and change pore fluid geochemistry significantly (Gieskes et al., 1982; Kastner and Siever, 1983;
129 Von Damm et al., 1985; Von Damm, 1990). At present, pore fluids in surface sediments show a
130 seawater composition (Geilert et al., 2018) and the absence of diagenetic high-temperature
131 processes render these pore fluids suitable for studying recent early diagenetic processes.

132

133 2.2 Sampling

134

135 Sediments were sampled via multicorer (MUC) deployment during RV SONNE cruise SO241 in
136 summer 2015 as described in detail in Geilert et al. (2018). In total, 6 stations have been investigated;
137 4 within the basin (termed basin sites: MUC33-11, MUC22-04, MUC23-05, MUC15-02), one in the
138 vicinity of a hydrothermal vent field (termed hydrothermal site: MUC66-16), and one within the OMZ
139 (termed OMZ site: MUC29-09) (Fig. 1, Table 1). The coring locations within the basin were sampled in



140 water depths between 1726 and 1855 m below sea level (mbsl). The hydrothermal site (MUC66-16)
141 was sampled in 1842 mbsl and was located at a distance of ~500 m from the active hydrothermal
142 mound described by Berndt et al. (2016). The OMZ site (MUC29-09) was sampled on the Guaymas
143 Basin slope of the Mexican mainland in 665 mbsl.

144 After core retrieval, bottom water above the sediment was sampled and filtered immediately using
145 0.2 μm cellulose acetate membrane filters. Bottom water from MUC22-04 may have been
146 contaminated with surface waters during core retrieval as indicated by Si and Mn concentrations
147 (53.8 μM and 0.05 μM , respectively) lower than at the remaining sites within the deep basin, which
148 show distinct anomalies caused by mixing with hydrothermal plume fluids (e.g. MUC15-02: Si = 177.8
149 μM and Mn = 0.34 μM). Processing of sediments was conducted in a cool laboratory in an argon-
150 flushed glove bag immediately after core retrieval. Sampling intervals were 1-5 cm with the highest
151 resolution close to the sediment surface and increasing distance downcore. Pore fluids were
152 separated from sediments by centrifugation (20 min at 4500 rpm) and subsequently filtered (0.2 μm
153 cellulose acetate membrane filters) for further analyses.

154

155 Water column samples were taken using a video-guided Niskin Water sampler CTD-Rosette System.
156 Water samples were taken in the basin above MUC15-02 at 1844 mbsl (VCTD02), within the
157 hydrothermal plume between 1781 and 1800 mbsl (VCTD06 and 09) above the Black Smoker mound
158 as described in Berndt et al. (2016), and above the OMZ site (MUC29-09) at 586 mbsl (Fig. 1).

159

160 2.3 bSiO₂ separation and digestion

161

162 The bSiO₂ mass fractions of sediment samples were determined using an automated leaching
163 method following Müller and Schneider (1993) at GEOMAR Helmholtz-Centre for Ocean Research
164 Kiel. The sample material was treated with 1M NaOH at 85°C to extract the opal fraction. The
165 increase in dissolved silica was monitored and evaluated using a method described by DeMaster
166 (1981). The precision of the mass fraction determination was 5 to 10% (1SD). The bSiO₂ was
167 separated from the sediment for Si isotope analyses following the method of Morley et al. (2004).
168 About 500 mg of a freeze-dried sediment sample was transferred into a centrifuge tube. Organic
169 matter and carbonate material was removed by adding H₂O₂ (Suprapur) and HCl, respectively. Clay
170 particles (grain size <2 μm) were separated from the remaining sediment by the Atterberg method
171 following Stoke's law (Müller, 1967). The remaining sediment (bSiO₂ and heavy minerals) was sieved
172 using a 5 μm -sieve and subsequently separated from the remaining detritus using heavy liquid
173 separation (sodium-polytungstate solution). The heavy liquid purification method was repeated until
174 clean, examined via light microscopy, bSiO₂ samples (>95%) were obtained. Light microscopy



175 revealed that the bSiO₂ fraction essentially consisted of diatoms and only traces of radiolarians and
176 sponges were present (<5%). The bSiO₂ samples were stored in Milli-Q water (MQ water). The bSiO₂
177 sample of the OMZ site stems from a nearby gravity core (GC07), which is described in detail in
178 Geilert et al. (2018). Aliquots of the cleaned bSiO₂ samples were transferred into Teflon vials and
179 dried on a hot plate. Subsequently, 1 ml of 0.1 M NaOH was added and the samples were placed on a
180 hot plate at 130°C for 24 hours. After sample digestion, the supernatant and residue (undissolved
181 traces of radiolarians and sponges) were separated via centrifugation. The supernatant was treated
182 with 200 µl H₂O₂ (Suprapur) in order to remove remaining organic matter and then dried and re-
183 dissolved in 1 ml 0.1 M NaOH at 130°C for 24 hours. After the digestion procedure, the samples were
184 diluted with MQ water and neutralized with 1 M HCl.

185

186 2.4 XRD measurements

187

188 X-ray diffraction analyses of the dried clay samples were performed at the Central Laboratory for
189 Crystallography and Applied Material Science, ZEKAM, dept. of Geosciences, University Bremen,
190 using a Philips X'Pert Pro multipurpose diffractometer. The diffractometer was equipped with a Cu-
191 tube, a fixed divergent slit of $\frac{1}{4}^\circ$, a secondary Ni filter, and a X'Celerator detector system. A
192 continuous scan from 3 to 85° 2θ was applied for the measurements with a calculated step size of
193 0.016° 2θ (calculated time per step was 50 seconds). Quantification of mineral phases were based on
194 the Philips software X'Pert High Score™, the freely available X-ray diffraction software MacDiff 4.25
195 (Petschick et al., 1996), and the QUAX full-pattern method after Vogt et al. (2002). The standard
196 deviation is ±1-3% for well crystallized minerals (see also Vogt et al., 2002) and ±5% for the remaining
197 mineral phases.

198

199 2.5 Geochemical analyses of fluid and solid phases

200

201 Analyses of major and trace element concentrations of pore fluids from the basin sites and the
202 hydrothermal site as well as the water column are described in Geilert et al. (2018). OMZ site pore
203 fluids were treated in the same way. In brief, the pore fluids were analysed onboard by photometry
204 (NH₄) and on shore for dissolved anions (Cl) and cations (Si, K, Na, Mg) using ion chromatography (IC,
205 METROHM 761 Compact, conductivity mode) and inductively coupled plasma optical emission
206 spectrometry (ICP-OES, VARIAN 720-ES), respectively. Analytical precision was constrained using the
207 IAPSO seawater standard for all chemical analyses (Gieskes et al., 1991) and was found to be <1% for
208 Cl, <2% for K, Na, Mg, and <5% for Si.

209



210 Freeze dried and ground sediment samples were digested in HF (40% Suprapur), HNO₃ (Suprapur),
211 and HClO₄ (60% p.a.) for major element analyses. The accuracy of the method was tested by method
212 blanks and the reference standards SDO-1 (Devonian Ohio Shale, USGS) and MESS-3 (Marine
213 Sediment Reference Material, Canadian Research Council). The digested samples were measured for
214 their K and Al contents by ICP-OES (VARIAN 720-ES) and reproducibility was ≤5%. Total carbon (TC)
215 and total organic carbon (TOC) were measured in freeze-dried and ground sediment samples by flash
216 combustion using the Carlo Erba Element Analyzer (NA-1500). Carbonate carbon (CaCO₃) was
217 calculated by subtracting TOC from TC.

218

219 The digested bSiO₂ samples were analyzed for their Al and Si contents using the Agilent 7500 series
220 quadrupole ICPMS at GEOMAR to provide information about potential clay contamination of the
221 separated bSiO₂ fraction (Shemesh et al., 1988), whereby Al/Si ratios below 50 mM/M are considered
222 as negligible clay contamination (van Bennekom et al., 1988; Hurd, 1973). Al/Si ratios in the studied
223 bSiO₂ ranged between 15 and 39 mM/M, with three exceptions in MUC22-04, MUC15-02, and
224 MUC66-16 yielding Al/Si ratios of 71 mM/M, 57 mM/M, 50 mM/M, respectively. However, all
225 $\delta^{30}\text{Si}_{\text{bSiO}_2}$ values agreed well with surrounding $\delta^{30}\text{Si}_{\text{bSiO}_2}$ values and clay contamination is thus
226 considered insignificant. All other bSiO₂ samples are considered clay-free.

227

228 2.6 Sample purification and Si isotope measurements

229

230 Fluid and digested bSiO₂ samples were prepared for Si isotope measurements following the
231 purification method of Georg et al. (2006b). The concentration of the samples was adjusted and
232 loaded (1 ml with ~64 μM Si) onto 1 ml pre-cleaned cation-exchange resin (Biorad AG50 W-X8) and
233 subsequently eluted with 2 ml MQ water. Matrix effects originating from dissolved organic
234 compounds and anions, which cannot be separated by this purification method, have previously
235 been found to potentially influence Si isotope measurements (van den Boorn et al., 2009; Hughes et
236 al., 2011). However, no influence of the matrix effects on pore fluid Si isotope measurements has
237 been found during our measurements following several tests described in Ehlert et al. (2016). Briefly,
238 Ehlert et al. (2016) removed organic compounds by H₂O₂ and SO₄ by Ba addition yielding $\delta^{30}\text{Si}$
239 values identical to untreated samples, within error. Therefore, our samples were not treated with
240 H₂O₂ or Ba before sample purification and Si isotope measurements.

241 Si isotope samples were measured in medium resolution on a NuPlasma MC-ICPMS (Nu
242 InstrumentsTM, Wrexham, UK) at GEOMAR using the Cetac Aridus II desolvator. Sample Si
243 concentrations of about 21 μM resulted in a ²⁸Si intensity of 3 to 4 V. The MQ blank was ≤ 3mV,
244 resulting in a blank to signal ratio <0.1 %. The measurements were performed using the standard-



245 sample bracketing method to account for mass bias drifts of the instrument (Albarède et al., 2004). Si
246 isotopes are reported in the $\delta^{30}\text{Si}$ notation, representing the deviation of the sample $^{30}\text{Si}/^{28}\text{Si}$ from
247 that of the international Si standard NBS28 in permil (‰). Long-term $\delta^{30}\text{Si}$ values of the reference
248 materials Big Batch ($-10.6\pm 0.2\text{‰}$; 2SD; $n=49$), IRMM018 ($-1.5\pm 0.2\text{‰}$; 2SD; $n=48$), Diatomite
249 ($+1.3\pm 0.2\text{‰}$; 2SD; $n=44$), and BHVO-2 ($-0.3\pm 0.2\text{‰}$; 2SD; $n=13$) are in good agreement with $\delta^{30}\text{Si}$
250 values in the literature (e.g. Reynolds et al., 2007; Zambardi and Poitrasson, 2011). The seawater
251 inter-calibration standard Aloha (1000 m) resulted in $+1.3\pm 0.2\text{‰}$ (2SD; $n=8$) in very good agreement
252 to Grasse et al. (2017). Additionally, two in-house matrix standards have been measured. The pore
253 fluid matrix standard yielded an average $\delta^{30}\text{Si}$ value of $+1.3\pm 0.2\text{‰}$ (2SD; $n=17$) and the diatom matrix
254 standard (*E. rex*) $-1.0\pm 0.2\text{‰}$ (2SD; $n=22$), which agrees well with earlier reported values (Ehlert et al.,
255 2016). All samples were measured 2-4 times on different days and the resulting $\delta^{30}\text{Si}$ values have
256 uncertainties between 0.1 and 0.4‰ (2SD, Table 1). The $\delta^{30}\text{Si}$ values of pore fluids, bSiO_2 , and bottom
257 water are given as $\delta^{30}\text{Si}_{\text{pf}}$, $\delta^{30}\text{Si}_{\text{bSiO}_2}$, and $\delta^{30}\text{Si}_{\text{bw}}$, respectively. Error bars in the figures indicate the
258 uncertainty of the individual sample measurements (two standard deviation, 2SD).

259

260 2.7 Numerical model

261

262 A numerical reactive-transport model was applied to simulate Si turnover within OMZ site sediments.
263 The model was based on a previously published Si isotope model (Ehlert et al., 2016) and was
264 extended to consider the dissolution of additional phases. A detailed description of the model can be
265 found in the supplementary information.

266

267 2.8 Calculation of the amount of terrigenous material and mass accumulation rate

268

269 The amount of terrigenous material (%) for the Guaymas Basin was calculated as the total mass
270 subtracted by the carbonate content (CaCO_3), the organic matter content (OC), and the bSiO_2 content
271 (Sayles et al., 2001):

272

$$273 \text{Terrigenous material} = 100 - (\text{CaCO}_3 + \text{OC} + \text{bSiO}_2) \quad (1)$$

274

275 The mass accumulation rate (MAR) was calculated as

276

$$277 \text{MAR} = S \cdot d \cdot (1 - \Phi) \quad (2)$$

278



279 with S the sedimentation rate as 0.18 cm yr^{-1} (Thunell et al., 1994) and d the bulk dry density as 2.5 g
280 cm^{-3} . The porosity (Φ) was taken at the deepest part of the core with 0.925.

281

282 3. RESULTS

283

284 3.1 Water chemistry and sediment composition

285

286 All water column, pore fluid, and hydrothermal Si concentration data, bSiO_2 weight fractions as well
287 as Si isotope values are reported in Tables 1 and 2. A detailed description of the water column
288 properties, pore fluids, and hydrothermal fluid chemistry can be found in Berndt et al. (2016) and
289 Geilert et al. (2018). Pore fluids predominantly show a seawater composition at all sampling sites and
290 are not influenced by high temperature processes related to sill intrusions or mixing with
291 hydrothermal fluids. Pore fluid geochemistry of major elements in the OMZ resembles that of the
292 remaining sampling sites with the exception of a strong enrichment in NH_4 (Table 1S and Geilert et
293 al., 2018) as well as high Fe and low Mn concentrations (Scholz et al., 2019). The porosity corrected K
294 (see supplement) and Al contents in the sediments ranged between 0.9 and 21.2 wt% and 2.9 and
295 66.6 wt%, respectively (Table 1). The TOC contents ranged between 0.3 and 7.8 % and are shown in
296 Table 1S.

297

298 3.2 Bottom water, water column, and hydrothermal fluid Si concentrations and $\delta^{30}\text{Si}$ values

299

300 The bottom water Si concentration ranged between 173 and 254 μM for all basin sites and the
301 hydrothermal site (between 1726 and 1855 mbsl) with the exception of MUC22-04, where Si
302 concentrations were as low as 54 μM (possible surface water contamination, see section 2.2 and
303 Table 1). The bottom water $\delta^{30}\text{Si}_{\text{bw}}$ signatures ranged between +1.5‰ and +2.0‰ for all basin sites
304 and the hydrothermal site and overlap within error (average $\delta^{30}\text{Si}_{\text{bw}}$: $+1.8 \pm 0.2\text{‰}$, 1SD; highest $\delta^{30}\text{Si}_{\text{bw}}$
305 for surface contaminated sample (MUC22-04)). Bottom water Si concentration for the OMZ site was
306 31 μM (665m water depth). The bottom water within the OMZ site had a distinctly lower $\delta^{30}\text{Si}_{\text{bw}}$
307 value of +0.8‰. Here, a potential contamination with surface waters can be excluded given that they
308 are characterized by high $\delta^{30}\text{Si}$ values (from 1.7 to 4.4‰; Ehlert et al., 2012; Grasse et al., 2013), due
309 to the preferential biological uptake of ^{28}Si (de la Rocha et al., 1997).

310

311 The basin water (VCTD02), which was sampled about 1 m above the seafloor, had a Si concentration
312 of 163 μM and a $\delta^{30}\text{Si}_{\text{deepBasin}}$ value of +1.5‰. Hydrothermal plume Si concentrations ranged between
313 253 and 690 μM and $\delta^{30}\text{Si}$ values ranged from +0.7‰ (VCTD09-06) to +1.4‰ (VCTD06-06). The water



314 column within the OMZ (586 mbsl) had a Si concentration of 78 μM and a $\delta^{30}\text{Si}_{\text{OMZ}}$ value of +1.5‰
315 (Table 2).

316

317 3.3 Pore fluid Si concentration and $\delta^{30}\text{Si}_{\text{pf}}$ values

318

319 Pore fluid Si concentrations generally increased asymptotically with depth from bottom water values
320 until reaching maximum average concentrations between 605 and 864 μM Si (Table 1, Fig. 2). For the
321 basin sites MUC33-11 and MUC15-02 as well as the OMZ site the Si concentrations asymptotically
322 increased until average values of 742 (≥ 8 cm below seafloor (cmbsf)), 729 (≥ 9 cmbsf), and 765 (≥ 9
323 cmbsf) μM were reached, respectively. Hydrothermal site Si concentrations were higher and
324 increased to 864 μM (≥ 4.5 cmbsf). MUC22-04 and MUC23-05 Si concentrations initially increased to
325 values of on average 605 μM (5.5 - 11 cmbsf) and 735 μM (3.5 - 9 cmbsf) and then decreased again to
326 364 μM (26 cmbsf) and 640 μM (22 cmbsf), respectively.

327

328 Pore fluid $\delta^{30}\text{Si}_{\text{pf}}$ values for all basin sites ranged from +0.9‰ to +1.5‰ (Table 1, Fig. 2), which is
329 lower than the respective bottom water $\delta^{30}\text{Si}_{\text{BW}}$ values ($\delta^{30}\text{Si}_{\text{BW}}$ from +1.6‰ to +2.0‰). The decrease
330 in Si concentration at MUC22-04 and MUC23-05 below 13 cmbsf and 11 cm cmbsf, respectively, is
331 not reflected in a significant change in $\delta^{30}\text{Si}_{\text{pf}}$. The hydrothermal site showed the highest $\delta^{30}\text{Si}_{\text{pf}}$ values
332 ranging from +1.8‰ and +2.2‰, which is higher than the bottom water $\delta^{30}\text{Si}_{\text{BW}}$ (+1.5‰). In contrast,
333 the OMZ site had the lowest $\delta^{30}\text{Si}_{\text{pf}}$ values between -0.5‰ and +0.8‰, which was also characterized
334 by very low $\delta^{30}\text{Si}_{\text{bw}}$ (+0.8‰; Table 1).

335

336 3.4 bSiO₂ content and $\delta^{30}\text{Si}_{\text{bSiO}_2}$ values

337

338 The bSiO₂ content of the sediments (Table 1, Fig. 2) varied between 4.7 wt% and 47.6 wt%. Lowest
339 contents were present at the basin site MUC22-04 (7.6 -13.1 wt%) and the hydrothermal site (4.7 -
340 14.6 wt%). The remaining sampling sites showed higher bSiO₂ contents of on average 23 \pm 7 wt%
341 (1SD). The $\delta^{30}\text{Si}_{\text{bSiO}_2}$ signatures ranged between +0.4‰ and +1.0‰ and did not vary systematically
342 with depth or sampling site within error. The small variability in $\delta^{30}\text{Si}_{\text{bSiO}_2}$ signatures most likely stems
343 from natural variability within the Guaymas Basin.

344

345 3.5 XRD results of the clay fraction

346

347 The main silicate mineral phases of all samples were phyllosilicates (16-59 wt%), primary silicates
348 (quartz, plagioclase, potassium feldspar; 15-38 wt%), and amorphous SiO₂ (4-43 wt% including



349 abiogenic and biogenic opal) (Table 2S). The phyllosilicates were mainly composed of variable
350 fractions of smectite, illite, montmorillonite, and kaolinite. Apart from silicate minerals, minor
351 amounts of Fe-(hydr)-oxides (≤ 10 wt%, most between 2 and 3 wt%), pyroxenes (≤ 8 wt%), and
352 carbonates (≤ 6 wt%) were present. Biogenic opal fragments were identified via light microscopy to
353 be the dominating amorphous silicate phase at all sites besides the hydrothermal site and MUC23-05
354 in the basin basin. At the hydrothermal site, the abiogenic amorphous silica fraction was the
355 dominating silica phase in the uppermost and lowermost core sections with only minor occurrences
356 of biogenic opal fragments. Abiogenic amorphous silica was also found in the uppermost and
357 lowermost core sections of MUC23-05.

358

359 4. DISCUSSION

360

361 Pore fluid Si concentration and $\delta^{30}\text{Si}_{\text{pf}}$ signatures vary significantly between sampling sites and appear
362 to depend strongly on ambient conditions. The Si concentration and isotope compositions are
363 proposed to be affected by dissolution of bSiO_2 , the dissolution of terrigenous phases, and the
364 formation of authigenic aluminosilicates; the latter process is defined as reverse weathering.
365 Dissolution of bSiO_2 is most effective in the reactive surface layer (≤ 10 cmbsf) where the degree of
366 silica undersaturation is highest. As soon as Si is released into solution via bSiO_2 dissolution, Si re-
367 precipitates as authigenic aluminosilicates as a function of the availability of reactive metals, made
368 available by dissolution of terrigenous material (e.g. Michalopoulos and Aller, 1995; Van Cappellen
369 and Qiu, 1997a,b; Loucaides et al., 2010). In the course of this process authigenic silicate
370 precipitation induces $\delta^{30}\text{Si}$ fractionation, whereby the ^{28}Si is preferentially incorporated into the solid
371 phase, enriching the remaining fluid in ^{30}Si (e.g. Georg et al., 2006a; Opfergelt et al., 2013; Ehlert et
372 al., 2016). In the following sections, the processes during early diagenesis influencing pore fluid
373 $\delta^{30}\text{Si}_{\text{pf}}$ signatures under different ambient conditions are discussed. For the OMZ site, we quantify
374 these processes using a reactive transport model and compare the results to the only other OMZ site
375 where pore fluid $\delta^{30}\text{Si}_{\text{pf}}$ data is available, the Peruvian margin.

376

377 4.1. Influences on $\delta^{30}\text{Si}_{\text{pf}}$ due to source mixing

378

379 In the open ocean, a strong correlation between the inverse Si concentration ($1/\text{Si}$) and Si isotope
380 composition in intermediate and deep waters exists, showing low $\delta^{30}\text{Si}$ values with high Si
381 concentrations and can be used to identify water mass mixing between two endmembers with
382 distinct Si characteristics (e.g. de Souza et al., 2012). Here, we use the two endmember mixing Eq. (3)



383 to calculate the mixing between the deep water column and fluids originating from bSiO₂ dissolution
384 according to

385

$$\delta^{30}\text{Si}_{mix} = \frac{(\delta^{30}\text{Si}_{\text{water column}} * [\text{Si}]_{\text{water column}} * f) + (\delta^{30}\text{Si}_{\text{bSiO}_2} * [\text{Si}]_{\text{bSiO}_2} * (1 - f))}{([\text{Si}]_{\text{water column}} * f) + ([\text{Si}]_{\text{bSiO}_2} * (1 - f))}$$

386 (3)

387 with $\delta^{30}\text{Si}_{\text{water column}}$ and $[\text{Si}]_{\text{water column}}$ as the respective water column Si isotope composition and
388 concentration (Table 2) and $\delta^{30}\text{Si}_{\text{bSiO}_2}$ as the average bSiO₂ value (+0.8‰) of all sites. The equilibrium
389 concentration in respect to bSiO₂ dissolution was derived from an experimental study by Van
390 Cappellen and Qiu (1997a) with $[\text{Si}]_{\text{bSiO}_2} = 900\mu\text{M}$. Mixing fractions are represented by f , varied over
391 100% water column and 0% fluids affected by bSiO₂ dissolution and vice versa.

392 Pore fluid $\delta^{30}\text{Si}_{\text{pf}}$ values of all sites deviate from mixing curves between the deep water column and
393 fluids originating from bSiO₂ dissolution and are obviously affected by additional processes (Fig. 3).
394 The $\delta^{30}\text{Si}_{\text{pf}}$ values of the basin sites and hydrothermal site are higher (+0.9‰ to +2.2‰) compared to
395 the respective mixing curves, while $\delta^{30}\text{Si}_{\text{pf}}$ values of the OMZ site are lower (-0.5‰ to +0.8‰). While
396 a shift to lower $\delta^{30}\text{Si}_{\text{pf}}$ values compared to fluid mixing point to dissolution of an isotopically light
397 phase, show higher $\delta^{30}\text{Si}_{\text{pf}}$ values that precipitation processes are important, given that the light Si
398 isotope is preferentially incorporated in authigenic secondary phases (Georg et al., 2009). This
399 indicates that processes governing the pore fluid Si isotope composition differ significantly between
400 the individual sites.

401

402 4.2. Influences on $\delta^{30}\text{Si}_{\text{pf}}$ from terrigenous and biogenic material

403

404 The terrigenous/bSiO₂ ratio was found to be the main mechanism controlling asymptotic pore fluid Si
405 concentration and the benthic Si flux (Van Cappellen and Qiu, 1997a, b). Maximum Si concentrations
406 were reached asymptotically at four out of six sampling sites (Fig. 2). Two sites within the basin
407 (MUC22-04 and MUC23-05) show lower Si concentrations in the deep core sections (Fig. 2), which
408 are most likely related to the decrease of reactive silica with depth, caused by the formation of less
409 soluble silica phases (Van Cappellen and Qiu, 1997a). At these sites, the asymptotic Si concentration
410 is defined as the maximum concentration values in the center of the core. The amount of terrigenous
411 material for the Guaymas Basin was calculated according to Eq. (1) and accounts for 75%.

412

413 Asymptotic Si concentrations plotted against the terrigenous/bSiO₂ ratio fall on the global trend
414 except for the hydrothermal site (Fig. 4a). Here, high geothermal gradients are likely responsible for
415 the higher Si concentrations with respect to the global trend (see also section 4.3.2). In contrast to



416 the asymptotic Si concentration, no strong correlation of the pore fluid $\delta^{30}\text{Si}_{\text{pf}}$ values with the
417 terrigenous/bSiO₂ ratio exists (Fig. 4b). In order to identify processes responsible for the different
418 pore fluid $\delta^{30}\text{Si}_{\text{pf}}$ values and to facilitate comparison between the three settings within the Guaymas
419 Basin, only average $\delta^{30}\text{Si}_{\text{pf}}$ values will be discussed in the following.

420

421 Average $\delta^{30}\text{Si}_{\text{pf}}$ values show distinct variations between the individual settings. The $\delta^{30}\text{Si}_{\text{pf}}$ values of
422 the OMZ site are lower ($0.0\pm 0.5\text{‰}$, 1SD, $n = 6$) than those of the basin sites ($+1.2\pm 0.1\text{‰}$, 1SD, $n = 17$)
423 and the hydrothermal site, which shows the highest $\delta^{30}\text{Si}_{\text{pf}}$ values ($+2.0\pm 0.2\text{‰}$, 1SD, $n = 3$).

424

425 4.3 Influence of the ambient environmental conditions on the $\delta^{30}\text{Si}_{\text{pf}}$ values

426

427 4.3.1 Basin sites

428

429 Pore fluid $\delta^{30}\text{Si}_{\text{pf}}$ values of the basin sites deviate from the mixing curve between the deep water
430 column and fluids originating from bSiO₂ dissolution and are shifted to higher values ($+1.2\pm 0.1\text{‰}$; Fig.
431 3). This shift to higher $\delta^{30}\text{Si}_{\text{pf}}$ values can be explained by Si re-precipitation as authigenic
432 aluminosilicates, which preferentially incorporate the light ²⁸Si isotope (Fig. 5a). Alteration of
433 terrigenous material leads to mobilization and re-precipitation of Al and the uptake of K from
434 seawater in the authigenic phase (Michalopoulos and Aller, 2004). The sedimentary K/Al ratio can
435 thus be used to detect these early diagenetic reactions in addition to pore fluid $\delta^{30}\text{Si}_{\text{pf}}$ values.
436 Authigenic aluminosilicates formed during alteration of terrigenous material were found to have K/Al
437 ratios of 0.32 (Michalopoulos and Aller, 2004), which is higher than the pristine K/Al ratio of
438 terrigenous material carried by rivers (K/Al = 0.19; Viers et al., 2009). The average K/Al ratio of the
439 basin sites is 0.34 ± 0.01 (1SD), which is in the same range as K/Al ratios indicative of authigenic
440 aluminosilicate formation (Michalopoulos and Aller, 2004). Thus, bSiO₂ dissolution and re-
441 precipitation of Si in authigenic aluminosilicates control the pore fluid $\delta^{30}\text{Si}_{\text{pf}}$ values in the basin sites.

442

443 4.3.2 Hydrothermal site

444

445 The $\delta^{30}\text{Si}_{\text{pf}}$ values from the hydrothermal site are higher ($+2.0\pm 0.2\text{‰}$) than the mixing curve between
446 the deep water column and fluids originating from bSiO₂ dissolution and also much higher than pore
447 fluid $\delta^{30}\text{Si}_{\text{pf}}$ values from the basin (Fig. 3, 5a). The high $\delta^{30}\text{Si}_{\text{pf}}$ values indicate that precipitation plays a
448 significant role at this site. Sedimentary K/Al ratios are equivalent to basin values (K/Al = 0.34) and
449 thus show the formation of authigenic aluminosilicates. Consequently, the higher pore fluid $\delta^{30}\text{Si}_{\text{pf}}$
450 values compared to the basin sites can either be explained by a different Si isotope fractionation



451 factor or by the precipitation of additional silica phases. The hydrothermal site is located in close
452 proximity to a hydrothermal vent field and hydrothermal deposits are mainly composed of Fe-
453 sulfides (Berndt et al., 2016), while nearby sediments are dominated by amorphous silica, quartz, and
454 Fe-Si silicates (e.g. ferrosilite, fayalite) (Kastner, 1982; Von Damm et al., 1985). Si adsorption to iron
455 (oxyhydr)oxide and incorporation into Fe-Si gels can create substantial Si isotope fractionation
456 (Delstanche et al., 2009; Zheng et al., 2016). Pore fluids show high Fe^{2+} concentrations (up to 190 μM ;
457 Scholz et al., 2019) and Si concentrations lower than amorphous Si and quartz solubilities at various
458 depths (this study; Von Damm et al., 1985; Gieskes et al., 1988), indicating precipitation of the
459 respective mineral phase during pore fluid ascent. Gieskes et al. (1988) reported on amorphous silica
460 cement in the hydrothermally-influenced sediments of the Guaymas Basin, which is supported by
461 findings of this study and likely explains the high amorphous SiO_2 contents identified by XRD (~35
462 wt%; see Sect. 3.5; Table 2S). In the Guaymas Basin, high thermal gradients (up to 11 K m^{-1} ; Geilert et
463 al., 2018) caused by igneous sill intrusions near the active spreading center significantly influence
464 diagenetic reactions at depth and accelerate Si dissolution and precipitation (Fig. 5a) (e.g. Kastner
465 and Siever, 1983). This can also explain the high pore fluid $\delta^{30}\text{Si}_{\text{pf}}$ values, given that deep Si saturated
466 fluids ascent and Si precipitates, likely along with Fe, over a large temperature range, whereby lower
467 temperatures are associated with larger Si isotope fractionation shifting pore fluid $\delta^{30}\text{Si}_{\text{pf}}$ to the
468 observed high values (Geilert et al., 2014; Zheng et al., 2016).

469

470 4.3.3 OMZ site

471

472 At the OMZ site, the $\delta^{30}\text{Si}_{\text{pf}}$ values are significantly lower (on average $0.0 \pm 0.5\text{‰}$) than the water
473 column $\delta^{30}\text{Si}_{\text{water column}}$ value ($+1.5 \pm 0.2\text{‰}$) and also lower than the $\delta^{30}\text{Si}_{\text{bSiO}_2}$ value ($+0.8\text{‰}$) (Fig. 2, 3).
474 Interestingly, the only other $\delta^{30}\text{Si}_{\text{pf}}$ values from an OMZ were obtained at the Peruvian margin (Ehlert
475 et al., 2016), where the $\delta^{30}\text{Si}_{\text{pf}}$ values are slightly higher than the water column $\delta^{30}\text{Si}_{\text{bw}}$ values ($+1.6\text{‰}$
476 and $+1.5\text{‰}$, respectively). As Ehlert et al. (2016) concluded, the Peruvian $\delta^{30}\text{Si}_{\text{pf}}$ values are influenced
477 by bSiO_2 dissolution and precipitation of authigenic aluminosilicates, the latter process shifting pore
478 fluid $\delta^{30}\text{Si}_{\text{pf}}$ to values higher than those of the water column. Consequently, in order to explain the
479 extremely low $\delta^{30}\text{Si}_{\text{pf}}$ values at the Guaymas Basin OMZ, an additional process must occur. We
480 hypothesize that a phase enriched in ^{28}Si needs to dissolve in order to shift the pore fluid $\delta^{30}\text{Si}_{\text{pf}}$
481 values and this phase might be 1) iron (oxyhydr)oxides with adsorbed ^{28}Si or 2) terrestrial clays.

482

483 Silicon exhibits a strong affinity to iron (oxyhydr)oxides (see also section 4.3.2; Davis et al., 2002) and
484 Si isotopes fractionate significantly during Si adsorption and co-precipitation (Delstanche et al., 2009;
485 Zheng et al., 2016). Dissolved Fe^{2+} in pore fluids can be transferred across the sediment-water



486 interface via diffusion and re-precipitates as iron (oxyhydr)oxides, where it subsequently dissolves
487 again in the reducing sediment. This process can repeat, resulting in multiple cycles of Fe dissolution
488 and re-precipitation on the Guaymas Basin slope (Scholz et al., 2019). We hypothesize that the light
489 ^{28}Si adsorbs to iron (oxyhydr)oxides in the water column and that upon reductive dissolution of Fe
490 minerals in the surface sediment, the light ^{28}Si isotope is re-released into the pore fluids, adding to
491 the observed low $\delta^{30}\text{Si}_{\text{pf}}$ values. However, the quantification of this Fe-Si shuttle and the contribution
492 to the low $\delta^{30}\text{Si}_{\text{pf}}$ values to the OMZ pore fluids remains difficult given that Fe undergoes multiple
493 cycles of dissolution and re-precipitation. Furthermore, the exact process of complexation, Si isotope
494 fractionation, and co-precipitation is unknown and requires further investigations. We can only
495 speculate that the transport of ^{28}Si via the Fe-Si shuttle is only of minor importance given that the
496 MAR of bSiO_2 and terrigenous material are dominating the Si supply to Guaymas OMZ sediments
497 (Calvert, 1966; DeMaster, 1981a).

498

499 The low $\delta^{30}\text{Si}_{\text{pf}}$ values can also be explained by dissolution of terrigenous clay particles, which are
500 generally enriched in ^{28}Si , showing a large range in $\delta^{30}\text{Si}$ with the majority between -3‰ to 0‰
501 (Frings et al., 2016 and references therein). Clays are usually considered to be the stable end product
502 of silicate weathering. However, fine clay particles and highly reactive surface sites of clays such as
503 montmorillonite, smectite and illite may dissolve in natural waters (Cappelli et al., 2018; Golubev et
504 al., 2006; Köhler et al., 2005). The dissolution is promoted by organic ligands and the reduction of
505 structural iron of clay minerals under reducing conditions (Anderson and Raiswell, 2004). Humic
506 substances that are abundant in OMZ sediments enriched in organic matter may catalyze the
507 microbial reduction of structural iron in clays (Lovley et al., 1998) and their dissolution (Liu et al.,
508 2017). Clays are abundant in OMZ sediments, given that fine-grained terrigenous material is
509 transported downslope from the shelf to the basin (Scholz et al., 2019). Furthermore, the microbial
510 oxidation of ferrous Fe in these fine-grained silicate minerals and its subsequent conversion to
511 reactive iron minerals was also found to contribute to the Fe cycling at the Guaymas Basin slope
512 (Scholz et al., 2019).

513

514 In order to constrain the possibility of terrigenous clay dissolution and the related shift to low $\delta^{30}\text{Si}_{\text{pf}}$
515 values in the Guaymas OMZ a reactive transport model was applied, based on our previously
516 published $\delta^{30}\text{Si}$ model (Ehlert et al., 2016). The data obtained at the Guaymas OMZ were used to
517 model the turnover of Si in these sediments and the previously published model extended to
518 consider additional processes (Fig. 6). A full description of the model is presented in the
519 supplementary information. The model was fit to dissolved silica concentrations and $\delta^{30}\text{Si}$ values
520 measured in pore fluids and biogenic opal and K/Al ratios determined in the solid phase (Fig. 6). High



521 rates of terrigenous clay dissolution were applied at the sediment surface to reproduce the observed
522 minima in $\delta^{30}\text{Si}_{\text{pf}}$ pore fluid values and K/Al ratios in a model run best fitting our data set (Fig. 6, best
523 fit). Since the terrigenous phases deposited at the sediment surface contain potassium ($K_{\text{terr}} = 1.7$
524 wt%, K/Al = 0.19; Viers et al., 2009) and are depleted in ^{30}Si (clay $\delta^{30}\text{Si} \approx -2\text{‰}$; Frings et al., 2016 and
525 references therein), the dissolution of these phases induces a decline in pore fluid $\delta^{30}\text{Si}$ and solid
526 phase K/Al (supplementary information). The precipitation of authigenic phases that are depleted in
527 ^{30}Si (Si isotoppe fractionation: $\Delta^{30}\text{Si}_{\text{au}} = -2\text{‰}$; Ehlert et al., 2016) and characterized by high K contents
528 (K/Al = 0.32; Michalopoulos and Aller, 2004) induces a down-core increase in pore fluid $\delta^{30}\text{Si}_{\text{pf}}$ and
529 solid phase K/Al below the surface minimum. Consequently, terrigenous clay dissolution under the
530 reducing conditions of the OMZ and subsequent authigenic aluminosilicate precipitation can explain
531 the low $\delta^{30}\text{Si}_{\text{pf}}$ values detected in Guaymas OMZ pore fluids (Fig. 5).

532

533 Additional simulations were conducted to investigate how the solid phase and pore fluid composition
534 is affected by the dissolution of terrigenous clay phases and the precipitation of authigenic phases
535 (Fig. 6). The surface minima in pore fluid $\delta^{30}\text{Si}_{\text{pf}}$ and solid phase K/Al disappear when the dissolution
536 rate is set to zero ($R_{\text{terr}} = 0$) while the ongoing precipitation of authigenic phases leads to a strong
537 down-core increase and high values at depth that are not consistent with the data. Pore fluid $\delta^{30}\text{Si}_{\text{pf}}$
538 and solid phase K/Al values strongly decrease with depth when the rate of authigenic phase
539 precipitation is set to zero ($R_{\text{au}} = 0$) such that the model yields values that are significantly lower than
540 the measured values. Dissolved silica concentrations cannot be used to further constrain R_{terr} and R_{au}
541 because they are largely controlled by the dissolution of biogenic opal (R_{opal}). Dissolved K
542 concentrations show a much lower sensitivity to R_{terr} and R_{au} than solid phase K/Al ratios due to the
543 high porosity of the OMZ sediments. Changes in dissolved K are largely eliminated by molecular
544 diffusion that is favored by the high porosity while the effect of the solid phase reactions R_{terr} and R_{au}
545 on the pore fluid composition is diminished by the low solid phase contents and the high background
546 concentration of dissolved K in ambient bottom waters. However, the model runs show that the
547 more sensitive pore fluid $\delta^{30}\text{Si}_{\text{pf}}$ and solid phase K/Al can be used to constrain the balance between
548 the dissolution of terrigenous phases and the precipitation of authigenic phases and that both
549 reactions are required to model the low $\delta^{30}\text{Si}_{\text{pf}}$ values measured in the Guaymas OMZ.

550

551 The modelled Si isotope composition of the benthic flux is -0.97‰ , which is lower than the $\delta^{30}\text{Si}$
552 value of the bottom water ($+0.8\text{‰}$). The higher bottom water $\delta^{30}\text{Si}$ value along with the low Si
553 concentration ($\sim 30\mu\text{M}$), which is lower than the ambient water column Si concentration ($\sim 80\mu\text{M}$),
554 indicates that a certain amount of Si must directly re-precipitate at the sediment water interface. Still
555 the $\delta^{30}\text{Si}$ of the bottom water is lower compared to the ambient water column, showing a benthic Si



556 flux with low $\delta^{30}\text{Si}$ values at continental margin settings, which is also in excellent agreement with
557 previously modelled and calculated $\delta^{30}\text{Si}$ values (Ehlert et al., 2016; Grasse et al., 2016). These
558 findings show that benthic Si fluxes at continental margins are a source of low $\delta^{30}\text{Si}$ values to the
559 ocean and need to be taken into account in future marine Si budget models.

560

561 4.4 Controlling processes and the impact on the global marine Si cycle

562

563 Stable and radioactive Si isotope data revealed significant sedimentary import and export processes
564 influencing the marine silica cycle (Ehlert et al., 2013, 2016; Tréguer and De La Rocha, 2013; Grasse
565 et al., 2016; Rahman et al., 2017; Sutton et al., 2018). Diatom burial removes about 9.9 Tmol yr^{-1} Si
566 from the ocean to the sediments, however, effects of terrigenous silicate dissolution and reverse
567 silicate weathering on bSiO_2 burial, preservation, and the benthic Si flux (and its Si isotope
568 composition) are not well constrained (Sutton et al., 2018). It has previously been shown that silicate
569 minerals dissolve in deep methanogenic sediments where the dissolution process is favored by high
570 CO_2 and organic ligand concentrations in ambient pore fluids (Wallmann et al., 2008). Similar to
571 chemical weathering on land, the dissolution of terrigenous silicate phases in marine sediments leads
572 to a release of cations and the conversion of CO_2 into HCO_3^- . Moreover, this marine weathering
573 process provides the dissolved Al that is needed for reverse weathering reactions. Our OMZ data
574 show for the first time that marine silicate weathering (dissolution of terrigenous silicates) also
575 occurs in OMZ surface sediments where it can outpace reverse weathering (precipitation of
576 authigenic silicates). Our study indicates that ambient environmental conditions appear to
577 significantly influence the balance between marine weathering and reverse weathering and thereby
578 the Si flux back to the ocean. Pore fluid $\delta^{30}\text{Si}_{\text{pf}}$ values depend on a complex interplay between bSiO_2 ,
579 terrigenous silicate dissolution, and authigenic aluminosilicate precipitation, however, the controlling
580 factors that determine which process dominates are difficult to constrain (Fig. 5). In view of the OMZ
581 settings (Guaymas Basin versus Peruvian margin), the most pronounced difference is the MAR_{terr}
582 which is significantly higher in the Guaymas Basin ($252 \text{ g m}^{-2} \text{ yr}^{-1}$; calculated by multiplying the
583 terrigenous content derived in Eq. (1) with the MAR from Eq. (2)) than at the Peruvian margin (100 g
584 $\text{m}^{-2} \text{ yr}^{-1}$; MAR from Ehlert et al., 2016; terrigenous content calculated after Eq. (1) with 6 wt% bSiO_2 ,
585 15 wt% OC, 8 wt% CaCO_3) (Fig. 5a, b). The high terrigenous detritus content is supplied via rivers in
586 the Guaymas Basin (Calvert, 1966; DeMaster, 1981). In combination with the high MAR_{terr} in the
587 Guaymas OMZ, high water/rock ratios (high porosity) additionally promote dissolution processes (Fig.
588 5). Lower MAR_{terr} and water/rock ratios found in the Peruvian upwelling margin appear to limit the
589 dissolution rate of terrigenous phases and promote authigenic aluminosilicate precipitation (Fig. 5b,
590 c), shifting pore fluid $\delta^{30}\text{Si}_{\text{pf}}$ to higher values compared to the corresponding $\delta^{30}\text{Si}_{\text{bSiO}_2}$ and $\delta^{30}\text{Si}_{\text{lbw}}$



591 values. This illustrates that the pore fluid $\delta^{30}\text{Si}_{\text{pr}}$ values of apparently similar settings (e.g. OMZ sites)
592 highly depend on the ambient environmental conditions and are not easily transferable.

593

594 4.5 Hydrothermal impact on the marine Si cycle

595

596 Findings of this study show that additional Si sources like hydrothermal input appear to affect the
597 oceanic $\delta^{30}\text{Si}$ values only in close vicinity to the hydrothermal fields. The $\delta^{30}\text{Si}$ values of the
598 hydrothermal plume (+0.7 to +1.4‰) are highly diluted by seawater ($\geq 94\%$, Table 2) and thus
599 deviate from hydrothermal fluid $\delta^{30}\text{Si}$ values (-0.3‰; De La Rocha et al., 2000). However, the
600 currently available data set regarding $\delta^{30}\text{Si}$ values of hydrothermal fluids is limited (two data points;
601 De La Rocha et al., 2000), even though they are in excellent agreement with oceanic crust $\delta^{30}\text{Si}$
602 values (-0.29±; Savage et al., 2010), the rock through which hydrothermal fluids circulate and gain
603 their Si isotopic signature. In our data set, no correlation exists between the $\delta^{30}\text{Si}$ values and the Si
604 concentration of the hydrothermal plume (Fig. 1S) and instead the $\delta^{30}\text{Si}$ values are predominantly
605 controlled by Si precipitation, likely in the hydrothermal conduit during ascent or after discharge in
606 contact with colder seawater. Temperature variations and interlinked precipitation rates were found
607 in addition to co-precipitation with Al or Fe to cause large Si fractionation such that precipitates are
608 enriched in ^{28}Si (Geilert et al., 2014, 2015; Oelze et al., 2015; Roerdink et al., 2015; Zheng et al.,
609 2016). The varying impacts of these factors can also explain why the diluted hydrothermal plume
610 $\delta^{30}\text{Si}$ values with the highest hydrothermal share (Table 2) does not show the lowest $\delta^{30}\text{Si}$ values,
611 indicative of hydrothermal fluids, given that Si is more reactive compared to Mg, the element on
612 which the hydrothermal share calculations are based (see supplement from Berndt et al., 2016). The
613 large range in hydrothermal plume $\delta^{30}\text{Si}$ values, which clearly show high degrees of seawater
614 dilution, illustrates the complexity of precipitation processes when hydrothermal fluids get in contact
615 with cold seawater and which requires further investigations especially with respect to the impact on
616 the global marine Si cycle.

617

618 5. CONCLUSIONS

619

620 Marine silicate weathering and reverse weathering impact the pore fluid isotopic composition of
621 sediments and are key processes of the marine silica cycle. In the Guaymas Basin, these processes
622 have been studied under markedly differing thermal and redox conditions. Si isotope compositions of
623 pore fluids combined with those of biogenic silica and ambient bottom waters helped to decipher
624 marine weathering and reverse weathering reactions, which would have remained undetected by
625 elemental concentrations alone and highlight the importance of Si isotope studies to constrain early



626 diagenetic reactions. Si concentrations and $\delta^{30}\text{Si}_{\text{pf}}$ signatures are the result of the interplay between
627 silica dissolution and Si precipitation, however, the involved phases differ significantly between the
628 study sites. Large differences in $\delta^{30}\text{Si}_{\text{pf}}$ values in a regionally constrained basin show that oxic/anoxic
629 conditions, hydrothermal fluids, water/rock ratios and the input of terrigenous material strongly
630 affect the pathways and turnover rates of Si in marine sediments. The light $\delta^{30}\text{Si}_{\text{pf}}$ and $\delta^{30}\text{Si}_{\text{BW}}$ values
631 from the Guaymas OMZ confirm earlier studies suggesting a light Si isotope value of the benthic Si
632 flux (Ehlert et al., 2016; Grasse et al., 2016), which need to be taken into account in future oceanic
633 mass balances of Si and in modelling studies concerning the isotopic Si cycle. Environmental settings,
634 in particular the MARS of terrigenous material, water/rock ratios, and redox conditions appear to be
635 the major factors controlling the balance between marine silicate weathering and reverse
636 weathering and the Si isotope fractionation in pore fluids of marine sedimentary settings and need to
637 be considered particularly in marine Si isotope studies.

638

639 AUTHOR CONTRIBUTION

640

641 SG, CH, MS, and FS helped sampling and processing of the samples onboard. SG, PG, and KD
642 conducted the Si isotope measurements. SG, CE, PG, KD, FS, and MF helped interpreting the data.
643 KW designed the reactive transport model. SG prepared the manuscript with the contribution of all
644 authors.

645

646 COMPETING INTEREST

647

648 The authors declare that they have no conflict of interest.

649

650 ACKNOWLEDGEMENTS

651

652 This work was part of the MAKS project funded by the German Ministry of Science and Education
653 (BMBF). We appreciate the support of the master and crew of the R/V Sonne during the SO241
654 cruise. We thank Regina Surberg, Bettina Domeyer, and Anke Bleyer for analytical support during the
655 cruise and on shore. Further thanks go to Tabitha Riff, Jutta Heinze, and Tyler Goepfert. Additional
656 support of this work was provided by EU-COST Action ES1301 "FLOWS" (www.flows-cost.eu) and the
657 German Collaborative Research Centre (SFB) 754: Climate – Biogeochemistry Interactions in the
658 Tropical Ocean funded by the German Science Foundation.

659

660



661 **References**

662

663 Abrantes, F., Lopes, C., Mix, A. and Pias, N.: Diatoms in Southeast Pacific surface sediments reflect
664 environmental properties, *Quat. Sci. Rev.*, 26(1–2), 155–169, doi:10.1016/j.quascirev.2006.02.022,
665 2007.

666 Albarède, F., Telouk, P., Blichert-Toft, J., Boyet, M., Agranier, A. and Nelson, B.: Precise and accurate
667 isotopic measurements using multiple-collector ICPMS, *Geochim. Cosmochim. Acta*, 68(12), 2725–
668 2744, doi:10.1016/j.gca.2003.11.024, 2004.

669 Anderson, T. F. and Raiswell, R.: SOURCES AND MECHANISMS FOR THE ENRICHMENT OF HIGHLY
670 REACTIVE IRON IN EUXINIC BLACK SEA SEDIMENTS, *Am. J. Sci.*, 304(March), 203–233, 2004.

671 Berndt, C., Hensen, C., Mortera-Gutierrez, C., Sarkar, S., Geilert, S., Schmidt, M., Liebetrau, V., Kipfer,
672 R., Scholz, F., Doll, M., Muff, S., Karstens, J., Planke, S., Petersen, S., Böttner, C., Chi, W.-C., Moser,
673 M., Behrendt, R., Fiskal, A., Lever, M. A., Su, C.-C., Deng, L., Brennwald, M. S. and Lizarralde, D.:
674 Rifting under steam – how rift magmatism triggers methane venting from sedimentary basins,
675 *Geology*, 44(9), 767–770, 2016.

676 Beucher, C. P., Brzezinski, M. A. and Jones, J. L.: Sources and biological fractionation of Silicon
677 isotopes in the Eastern Equatorial Pacific, *Geochim. Cosmochim. Acta*, 72(13), 3063–3073,
678 doi:10.1016/j.gca.2008.04.021, 2008.

679 Beucher, C. P., Brzezinski, M. A. and Jones, J. L.: Mechanisms controlling silicon isotope distribution in
680 the Eastern Equatorial Pacific, *Geochim. Cosmochim. Acta*, 75(15), 4286–4294,
681 doi:10.1016/j.gca.2011.05.024, 2011.

682 Bruland, K. W., Rue, E. L., Smith, G. J. and DiTullio, G. R.: Iron, macronutrients and diatom blooms in
683 the Peru upwelling regime: Brown and blue waters of Peru, *Mar. Chem.*, 93(2–4), 81–103,
684 doi:10.1016/j.marchem.2004.06.011, 2005.

685 Calvert, S. E.: Factors affecting distribution of laminated diatomaceous sediments in Gulf of
686 California, in *Marine Geology of Gulf of California*, edited by T. van Andel and G. G. Shor, pp. 311–
687 330, *Am Assoc. Petrol. Geol. Mem.*3., 1964.

688 Calvert, S. E.: Accumulation of Diatomaceous Silica in the Sediments of the Gulf of California, *Geol.*
689 *Soc. Am. Bull.*, 77(June), 569–596, 1966.

690 Campbell, A. C. and Gieskes, J. M.: Water column anomalies associated with hydrothermal activity in
691 the Guaymas Basin, Gulf of California Andrew C. Campbell and Joris M. Gieskes, *Earth Planet. Sci.*
692 *Lett.*, 68, 57–72, 1984.

693 Cappelli, C., Yokoyama, S., Cama, J. and Huertas, F. J.: Montmorillonite dissolution kinetics:
694 Experimental and reactive transport modeling interpretation, *Geochim. Cosmochim. Acta*, 227, 96–
695 122, 2018.



696 Cardinal, D., Alleman, L. Y., Dehairs, F., Savoye, N., Trull, T. W. and André, L.: Relevance of silicon
697 isotopes to Si-nutrient utilization and Si-source assessment in Antarctic waters, *Global Biogeochem.*
698 *Cycles*, 19(2), 1–13, doi:10.1029/2004GB002364, 2005.

699 Curray, J. R. and Moore, D. G. et al.: Initial Reports of the Deep Sea Drilling Project. vol. 64., U.S.
700 Govt. Printing Office, Washington., 1982.

701 Davis, C. C., Chen, H. W. and Edwards, M.: Modeling silica sorption to iron hydroxide, *Environ. Sci.*
702 *Technol.*, 36(4), 582–587, doi:10.1021/es010996t, 2002.

703 De La Rocha, C. L., Brzezinski, M. A. and DeNiro, M. J.: Fractionation of silicon isotopes by marine
704 diatoms during biogenic silica formation, *Geochim. Cosmochim. Acta*, 61(23), 5051–5056,
705 doi:10.1016/S0016-7037(97)00300-1, 1997.

706 De La Rocha, C. L., Brzezinski, M. A. and Deniro, M. J.: A first look at the distribution of the stable
707 isotopes of silicon in natural waters, *Geochim. Cosmochim. Acta*, 64(14), 2467–2477,
708 doi:10.1016/S0016-7037(00)00373-2, 2000.

709 Delstanche, S., Opfergelt, S., Cardinal, D., Elsass, F., André, L. and Delvaux, B.: Silicon isotopic
710 fractionation during adsorption of aqueous monosilicic acid onto iron oxide, *Geochim. Cosmochim.*
711 *Acta*, 73(4), 923–934, doi:10.1016/j.gca.2008.11.014, 2009.

712 DeMaster, D. J.: The supply and accumulation of silica in the marine environment., *Geochemica*
713 *Cosmochim. Acta*, 45, 1715–1732, 1981.

714 de Souza, G. F., Reynolds, B. C., Rickli, J., Frank, M., Saito, M. A., Gerringa, L. J. A. and Bourdon, B.:
715 Southern Ocean control of silicon stable isotope distribution in the deep Atlantic Ocean, *Global*
716 *Biogeochem. Cycles*, 26(2), 1–13, doi:10.1029/2011GB004141, 2012.

717 de Souza, G. F., Slater, R. D., Dunne, J. P. and Sarmiento, J. L.: Deconvolving the controls on the deep
718 ocean’s silicon stable isotope distribution, *Earth Planet. Sci. Lett.*, 398, 66–76,
719 doi:10.1016/j.epsl.2014.04.040, 2014.

720 de Souza, G. F., Slater, R. D., Hain, M. P., Brzezinski, M. A. and Sarmiento, J. L.: Distal and proximal
721 controls on the silicon stable isotope signature of North Atlantic Deep Water, *Earth Planet. Sci. Lett.*,
722 432, 342–353, doi:10.1016/j.epsl.2015.10.025, 2015.

723 Dixit, S., Van Cappellen, P. and van Bennekom, a J.: Processes controlling solubility of biogenic silica
724 and pore water build-up of silicic acid in marine sediments, *Mar. Chem.*, 73, 333–352, 2001.

725 Ehlert, C., Grasse, P., Mollier-Vogel, E., Bösch, T., Franz, J., de Souza, G. F., Reynolds, B. C.,
726 Stramma, L. and Frank, M.: Factors controlling the silicon isotope distribution in waters and surface
727 sediments of the Peruvian coastal upwelling, *Geochim. Cosmochim. Acta*, 99, 128–145,
728 doi:10.1016/j.gca.2012.09.038, 2012.

729 Ehlert, C., Grasse, P. and Frank, M.: Changes in silicate utilisation and upwelling intensity off Peru
730 since the Last Glacial Maximum - insights from silicon and neodymium isotopes, *Quat. Sci. Rev.*, 72,



- 731 18–35, doi:10.1016/j.quascirev.2013.04.013, 2013.
- 732 Ehlert, C., Doering, K., Wallmann, K., Scholz, F., Sommer, S., Grasse, P., Geilert, S. and Frank, M.:
733 Stable silicon isotope signatures of marine pore waters – Biogenic opal dissolution versus authigenic
734 clay mineral formation, *Geochim. Cosmochim. Acta*, 191, 102–117, doi:10.1016/j.gca.2016.07.022,
735 2016.
- 736 Frings, P. J., Clymans, W., Fontorbe, G., De La Rocha, C. L. and Conley, D. J.: The continental Si cycle
737 and its impact on the ocean Si isotope budget, *Chem. Geol.*, 425, 12–36,
738 doi:10.1016/j.chemgeo.2016.01.020, 2016.
- 739 Geilert, S., Vroon, P. Z., Roerdink, D. L., Cappellen, P. Van and van Bergen, M. J.: Silicon isotope
740 fractionation during abiotic silica precipitation at low temperatures: inferences from flow-through
741 experiments, *Geochim. Cosmochim. Acta*, 142, 95–114, doi:10.1016/j.gca.2014.07.003, 2014.
- 742 Geilert, S., Vroon, P. Z., Keller, N. S., Gudbrandsson, S., Stefánsson, A. and van Bergen, M. J.: Silicon
743 isotope fractionation during silica precipitation from hot-spring waters: Evidence from the Geysir
744 geothermal field, Iceland, *Geochim. Cosmochim. Acta*, 164, doi:10.1016/j.gca.2015.05.043, 2015.
- 745 Geilert, S., Vroon, P. Z. and van Bergen, M. J.: Effect of diagenetic phase transformation on the silicon
746 isotope composition of opaline sinter deposits of Geysir, Iceland, *Chem. Geol.*, 433,
747 doi:10.1016/j.chemgeo.2016.04.008, 2016.
- 748 Geilert, S., Hensen, C., Schmidt, M., Liebetrau, V., Scholz, F., Doll, M., Deng, L., Fiskal, A., Lever, M. A.,
749 Su, C.-C., Schlömer, S., Sarkar, S., Thiel, V. and Berndt, C.: On the formation of hydrothermal vents
750 and cold seeps in the Guaymas Basin, Gulf of California, *Biogeosciences*, 15, 5715–5731 [online]
751 Available from: <https://doi.org/10.5194/bg-15-5715-2018>, 2018.
- 752 Georg, R. B., Reynolds, B. C., Frank, M. and Halliday, A. N.: Mechanisms controlling the silicon
753 isotopic compositions of river waters, *Earth Planet. Sci. Lett.*, 249(3–4), 290–306,
754 doi:10.1016/j.epsl.2006.07.006, 2006a.
- 755 Georg, R. B., Reynolds, B. C., Frank, M. and Halliday, A. N.: New sample preparation techniques for
756 the determination of Si isotopic compositions using MC-ICPMS, *Chem. Geol.*, 235(1–2), 95–104,
757 doi:10.1016/j.chemgeo.2006.06.006, 2006b.
- 758 Georg, R. B., Zhu, C., Reynolds, B. C. and Halliday, A. N.: Stable silicon isotopes of groundwater,
759 feldspars, and clay coatings in the Navajo Sandstone aquifer, Black Mesa, Arizona, USA, *Geochim.*
760 *Cosmochim. Acta*, 73(8), 2229–2241, doi:10.1016/j.gca.2009.02.005, 2009.
- 761 Gieskes, J. M., Kastner, M., Einsele, G., Kelts, K. and Niemitz, J.: Hydrothermal Activity in the Guaymas
762 Basin, Gulf of California: A synthesis, in *Initial Reports of the Deep Sea Drilling Project*. vol. 64, Pt.
763 2, edited by J. Blakeslee, L. W. Platt, and L. N. Stout, pp. 1159–1167., 1982.
- 764 Gieskes, J. M., Simoneit, B. R. T., Brown, T., Shaw, T., Wang, Y. C. and Magenheimer, A.: Hydrothermal
765 fluids and petroleum in surface sediments of Guaymas Basin, Gulf of California: A case study, *Can.*



- 766 Mineral., 26, 589–602 [online] Available from:
767 <http://canmin.geoscienceworld.org/cgi/reprint/26/3/589>, 1988.
- 768 Gieskes, J. M., Gamo, T. and Brumsack, H.: Chemical methods for interstitial water analysis aboard
769 Joides Resolution, Ocean Drill. Prog. Tech. Note 15. Texas A&M Univ. Coll. Stn., 1991.
- 770 Golubev, S. V, Bauer, A. and Pokrovsky, O. S.: Effect of pH and organic ligands on the kinetics of
771 smectite dissolution at 25 ° C, *Geochim. Cosmochim. Acta*, 70, 4436–4451,
772 doi:10.1016/j.gca.2006.06.1557, 2006.
- 773 Grasse, P., Ehlert, C. and Frank, M.: The influence of water mass mixing on the dissolved Si isotope
774 composition in the Eastern Equatorial Pacific, *Earth Planet. Sci. Lett.*, 380, 60–71,
775 doi:10.1016/j.epsl.2013.07.033, 2013.
- 776 Grasse, P., Ryabenko, E., Ehlert, C., Altabet, M. A. and Frank, M.: Silicon and nitrogen cycling in the
777 upwelling area off Peru: A dual isotope approach, *Limnol. Oceanogr.*, 61(5), 1661–1676,
778 doi:10.1002/lno.10324, 2016.
- 779 Grasse, P., Brzezinski, M. A., Cardinal, D., de Souza, G. F., Andersson, P., Closset, I., Cao, Z., Dai, M.,
780 Ehlert, C., Estrade, N., François, R., Frank, M., Jiang, G., Jones, J. L., Kooijman, E., Liu, Q., Lu, D.,
781 Pahnke, K., Ponzevera, E., Schmitt, M., Sun, X., Sutton, J. N., Thil, F., Weis, D., Wetzel, F., Zhang, A.,
782 Zhang, J. and Zhang, Z.: GEOTRACES inter-calibration of the stable silicon isotope composition of
783 dissolved silicic acid in seawater, *J. Anal. At. Spectrom.*, 32(3), 562–578, doi:10.1039/C6JA00302H,
784 2017.
- 785 Hughes, H. J., Delvigne, C., Korntheuer, M., de Jong, J., André, L. and Cardinal, D.: Controlling the
786 mass bias introduced by anionic and organic matrices in silicon isotopic measurements by MC-ICP-
787 MS, *J. Anal. At. Spectrom.*, 26(9), 1892, doi:10.1039/c1ja10110b, 2011.
- 788 Hurd, D. C.: Interactions of biogenic opal , sediment and seawater in the Central Equatorial Pacific,
789 *Geochemica Cosmochim. Acta*, 37, 2257–2282, 1973.
- 790 Kastner, M.: Evidence for Two Distinct Hydrothermal Systems in the Guaymas Basin, in *In Initial*
791 *Reports of the Deep Sea Drilling Project. vol. 64, Pt. 2*, edited by J. Blakeslee, L. W. Platt, and L. N.
792 Stout, pp. 1143–1157, U.S. Govt. Printing Office, Washington., 1982.
- 793 Kastner, M. and Siever, R.: Siliceous Sediments of the Guaymas Basin: The Effect of High Thermal
794 Gradients on Diagenesis, *J. Geol.*, 91(6), 629–641, doi:10.1086/628816, 1983.
- 795 Köhler, S. J., Bosbach, D. B. and Oelkers, E. H.: Do clay mineral dissolution rates reach steady state?,
796 *Geochim. Cosmochim. Acta*, 69(8), 1997–2006, doi:10.1016/j.gca.2004.10.015, 2005.
- 797 Lewin, J. C.: The dissolution of silica from diatom walls, *Geochim. Cosmochim. Acta*, 21(3–4), 182–
798 198, doi:10.1016/S0016-7037(61)80054-9, 1961.
- 799 Liu, G., Qiu, S., Liu, B., Pu, Y., Gao, Z., Wang, J., Jin, R. and Zhou, J.: Microbial reduction of Fe(III)-
800 bearing clay minerals in the presence of humic acids, *Sci. Rep.*, 7(9), doi:10.1038/srep45354, 2017.



- 801 Loucaides, S., Michalopoulos, P., Presti, M., Koning, E., Behrends, T. and Van Cappellen, P.: Seawater-
802 mediated interactions between diatomaceous silica and terrigenous sediments: Results from long-
803 term incubation experiments, *Chem. Geol.*, 270(1–4), 68–79, doi:10.1016/j.chemgeo.2009.11.006,
804 2010.
- 805 Lovley, D. R., Fraga, J. L., Blunt-Harris, E. L., Hayes, L. A., Phillips, E. J. P. and Coates, J. D.: Humic
806 Substances as a Mediator for Microbially Catalyzed Metal Reduction, *Acta Hydrochim. hydrobiol*, 26,
807 152–157, 1998.
- 808 Lupton, J. E.: Helium-3 in the Guaymas Basin: Evidence for injection of mantle volatiles in the Gulf of
809 California, *J. Geophys. Res.*, 84(B13), 7446, doi:10.1029/JB084iB13p07446, 1979.
- 810 Mackenzie, F. T., Ristvet, B. ., Thorstenson, D. C., Lerman, A. and Leeper, R. H.: Reverse weathering
811 and chemical mass balance in a coastal environment, in *River Inputs to Ocean Systems*, edited by J.
812 M. Marten, J. D. Burton, and D. Eisma, pp. 152–187, UNEP and UNESCO, Switzerland., 1981.
- 813 McManus, J., Hammond, D. E., Berelson, W. M., Kilgore, T. E., Demaster, D. J., Ragueneau, O. G. and
814 Collier, R. W.: Early diagenesis of biogenic opal: Dissolution rates, kinetics, and paleoceanographic
815 implications, *Deep. Res. Part II*, 42(2–3), 871–903, doi:10.1016/0967-0645(95)00035-O, 1995.
- 816 Méheut, M., Lazzeri, M., Balan, E. and Mauri, F.: Equilibrium isotopic fractionation in the kaolinite,
817 quartz, water system: Prediction from first-principles density-functional theory, *Geochim.*
818 *Cosmochim. Acta*, 71(13), 3170–3181, doi:10.1016/j.gca.2007.04.012, 2007.
- 819 Michalopoulos, P. and Aller, R. C.: Rapid Clay Mineral Formation in Amazon Delta Sediments: Reverse
820 Weathering and Oceanic Elemental Cycles, *Science*, 270(5236), 614–617,
821 doi:10.1126/science.270.5236.614, 1995.
- 822 Michalopoulos, P. and Aller, R. C.: Early diagenesis of biogenic silica in the Amazon delta: Alteration,
823 authigenic clay formation, and storage, *Geochim. Cosmochim. Acta*, 68(5), 1061–1085,
824 doi:10.1016/j.gca.2003.07.018, 2004.
- 825 Michalopoulos, P., Aller, R. C. and Reeder, R. J.: Conversion of diatoms to clays during early
826 diagenesis in tropical, continental shell muds, *Geology*, 28(12), 1095–1098, doi:10.1130/0091-
827 7613(2000)28<1095:CODTCD>2.0.CO, 2000.
- 828 Morley, D. W., Leng, M. J., Mackay, A. W., Sloane, H. J., Rioual, P. and Battarbee, R. W.: Cleaning of
829 lake sediment samples for diatom oxygen isotope analysis, *J. Paleolimnol.*, 31(3), 391–401,
830 doi:10.1023/B:JOPL.0000021854.70714.6b, 2004.
- 831 Müller, G.: *Methods in sedimentary petrology.*, in *Sedimentary Petrology, Volume 1*, edited by W.
832 von Engelhardt, H. Füchtbauer, and G. Müller, pp. 1–283, Schweizerbart, Stuttgart, Germany., 1967.
- 833 Müller, P. J. and Schneider, R.: An automated leaching method for the determination of opal in
834 sediments and particulate matter, *Deep. Res. Part I*, 40(3), 425–444, doi:10.1016/0967-
835 0637(93)90140-X, 1993.



- 836 Ng, C. H., Cassarino, L., Pickering, R. A., Woodward, E. M. S., Hammond, S. J. and Hendry, K. R.:
837 Sediment efflux of silicon on the Greenland margin and implications for the marine silicon cycle,
838 *Earth Planet. Sci. Lett.*, 529, 115877, doi:10.1016/j.epsl.2019.115877, 2020.
- 839 Oelze, M., von Blanckenburg, F., Bouchez, J., Hoellen, D. and Dietzel, M.: The effect of Al on Si isotope
840 fractionation investigated by silica precipitation experiments, *Chem. Geol.*, 397, 94–105,
841 doi:10.1016/j.chemgeo.2015.01.002, 2015.
- 842 Opfergelt, S., Burton, K. W., Pogge von Strandmann, P. a E., Gislason, S. R. and Halliday, a. N.:
843 Riverine silicon isotope variations in glaciated basaltic terrains: Implications for the Si delivery to the
844 ocean over glacial-interglacial intervals, *Earth Planet. Sci. Lett.*, 369–370, 211–219,
845 doi:10.1016/j.epsl.2013.03.025, 2013.
- 846 Petschick, R., Kuhn, G. and Gingele, F.: Clay mineral distribution in surface sediments of the South
847 Atlantic: sources, transport, and relation to oceanography, *Mar. Geol.*, 130(3–4), 203–229,
848 doi:10.1016/0025-3227(95)00148-4, 1996.
- 849 Rabouille, C., Gaillard, J. F., Tréguer, P. and Vincendeau, M. A.: Biogenic silica recycling in surficial
850 sediments across the Polar Front of the Southern Ocean (Indian Sector), *Deep. Res. Part II Top. Stud.*
851 *Oceanogr.*, 44(5), 1151–1176, doi:10.1016/S0967-0645(96)00108-7, 1997.
- 852 Ragueneau, O., Tréguer, P., Leynaert, A., Anderson, R. F., Brzezinski, M. A., DeMaster, D. J., Dugdale,
853 R. C., Dymond, J., Fischer, G., François, R., Heinze, C., Maier-Reimer, E., Martin-Jézéquel, V., Nelson,
854 D. M. and Quéguiner, B.: A review of the Si cycle in the modern ocean: Recent progress and missing
855 gaps in the application of biogenic opal as a paleoproductivity proxy, *Glob. Planet. Change*, 26(4),
856 317–365, doi:10.1016/S0921-8181(00)00052-7, 2000.
- 857 Rahman, S., Aller, R. C. and Cochran, J. K.: The Missing Silica Sink: Revisiting the Marine Sedimentary
858 Si Cycle Using Cosmogenic³²Si, *Global Biogeochem. Cycles*, 31(10), 1559–1578,
859 doi:10.1002/2017GB005746, 2017.
- 860 Reynolds, B. C., Aggarwal, J., André, L., Baxter, D., Beucher, C., Brzezinski, M. A., Cardinal, D.,
861 Engström, E., Georg, R. B., Land, M., Leng, M. J., Opfergelt, S., Rodushkin, I., Sloane, H. J., van den
862 Boorn, S. H. J. M., Vroon, P. Z. and Cardinal, D.: An inter-laboratory comparison of Si isotope
863 reference materials, *J. Anal. Atom. Spectrom.*, 22, 561–568, doi:10.1039/b616755a, 2007.
- 864 Rickert, D.: Dissolution kinetics of biogenic silica in marine environments, *Ber. Polarforschung*, 351
865 [online] Available from: ISSN 0176-5027, 2000.
- 866 Rickert, D., Schlüter, M. and Wallmann, K.: Dissolution kinetics of biogenic silica from the water
867 column to the sediments, *Geochim. Cosmochim. Acta*, 66(3), 439–455, doi:10.1016/S0016-
868 7037(01)00757-8, 2002.
- 869 Roerdink, D. L., van den Boorna, S. H. J. M., Geilert, S., Vroon, P. Z. and van Bergen, M. J.:
870 Experimental constraints on kinetic and equilibrium silicon isotope fractionation during the



- 871 formation of non-biogenic chert deposits, *Chem. Geol.*, 402, 40–51,
872 doi:10.1016/j.chemgeo.2015.02.038, 2015.
- 873 Savage, P. S., Georg, R. B., Armytage, R. M. G., Williams, H. M. and Halliday, A. N.: Silicon isotope
874 homogeneity in the mantle, *Earth Planet. Sci. Lett.*, 295(1–2), 139–146,
875 doi:10.1016/j.epsl.2010.03.035, 2010.
- 876 Sayles, F. L., Martin, W. R., Chase, Z. and Anderson, R. F.: Benthic remineralization and burial of
877 biogenic SiO₂, CaCO₃, organic carbon, and detrital material in the Southern Ocean along a transect
878 at 170° West, *Deep. Res. Part II*, 48, 4323–4383, 2001.
- 879 Scholz, F., Schmidt, M., Hensen, C., Geilert, S., Gutjahr, M. and Liebetrau, V.: Shelf-to-basin iron
880 shuttle in the Guaymas Basin, Gulf of California, *Geochim. Cosmochim. Acta*, 261, 76–92,
881 doi:10.1016/j.gca.2019.07.006, 2019.
- 882 Shemesh, A., Mortlock, R. A., Smith, R. J. and Froelich, P. N.: Determination of Ge/Si in Marine
883 Siliceous Microfossils: Separation, Cleaning and Dissolution of Diatoms and Radiolaria, *Mar. Chem.*,
884 25, 305–323, 1988.
- 885 Sutton, J. N., Varela, D. E., Brzezinski, M. A. and Beucher, C. P.: Species-dependent silicon isotope
886 fractionation by marine diatoms, *Geochim. Cosmochim. Acta*, 104, 300–309,
887 doi:10.1016/j.gca.2012.10.057, 2013.
- 888 Sutton, J. N., André, L., Cardinal, D., Conley, D. J., de Souza, G. F., Dean, J., Dodd, J., Ehlert, C.,
889 Ellwood, M. J., Frings, P. J., Grasse, P., Hendry, K., Leng, M. J., Michalopoulos, P., Panizzo, V. N. and
890 Swann, G. E. A.: A Review of the Stable Isotope Bio-geochemistry of the Global Silicon Cycle and Its
891 Associated Trace Elements, *Front. Earth Sci.*, 5(January), doi:10.3389/feart.2017.00112, 2018.
- 892 Tatzel, M., von Blanckenburg, F., Oelze, M., Schuessler, J. A. and Bohrmann, G.: The silicon isotope
893 record of early silica diagenesis, *Earth Planet. Sci. Lett.*, 428, 293–303,
894 doi:10.1016/j.epsl.2015.07.018, 2015.
- 895 Teske, A., Callaghan, A. V. and LaRowe, D. E.: Biosphere frontiers of subsurface life in the sedimented
896 hydrothermal system of Guaymas Basin, *Front. Microbiol.*, 5(JULY), 1–11,
897 doi:10.3389/fmicb.2014.00362, 2014.
- 898 Thunell, R. C., Pride, C. J., Tappa, E. and Muller-Karger, F. E.: Biogenic silica fluxes and accumulation
899 rates in the Gulf of California, *Geology*, 22(April), 303–306, doi:10.1130/0091-7613(1994)022<0303,
900 1994.
- 901 Tréguer, P. and Pondaven, P.: Silica control of carbon dioxide, *Nature*, 406, 358–359,
902 doi:10.1080/00207238608710255, 2000.
- 903 Tréguer, P. J. and De La Rocha, C. L.: The World Ocean Silica Cycle, *Ann. Rev. Mar. Sci.*, 5(1),
904 120725114348000, doi:10.1146/annurev-marine-121211-172346, 2013.
- 905 van Bennekom, A. J., Berger, G. W., Van Der Gaast, S. J. and De Vries, R. T. P.: PRIMARY



- 906 PRODUCTIVITY AND THE SILICA CYCLE IN THE SOUTHERN OCEAN (ATLANTIC SECTOR), *Palaeogeogr.*
907 *Palaeoclim. Palaeoecol.*, 67, 19–30, 1988.
- 908 Van Cappellen, P. and Qiu, L. Q.: Biogenic silica dissolution in sediments of the Southern Ocean.1.
909 Solubility, *Deep. Res. Part II-Topical Stud. Oceanogr.*, 44(5), 1109–1128, doi:10.1016/S0967-
910 0645(96)00113-0, 1997a.
- 911 Van Cappellen, P. and Qiu, L.: Biogenic silica dissolution in sediments of the Southern Ocean . II
912 Kinetics, *Deep. Res. II*, 44(5), 1129–1149, 1997b.
- 913 van den Boorn, S. H. J. M., Vroon, P. Z. and van Bergen, M. J.: Sulfur-induced offsets in MC-ICP-MS
914 silicon-isotope measurements, *J. Anal. At. Spectrom.*, 24(8), 1111, doi:10.1039/b816804k, 2009.
- 915 Varela, D. E.: Biological fractionation of silicon isotopes in Southern Ocean surface waters, *Global*
916 *Biogeochem. Cycles*, 18(1), 1–8, doi:10.1029/2003GB002140, 2004.
- 917 Viers, J., Dupré, B. and Gaillardet, J.: Chemical composition of suspended sediments in World Rivers :
918 New insights from a new database, *Sci. Total Environ.*, 407(2), 853–868,
919 doi:10.1016/j.scitotenv.2008.09.053, 2009.
- 920 Vogt, C., Lauterjung, J. and Fischer, R. X.: INVESTIGATION OF THE CLAY FRACTION (<2µm) OF THE
921 CLAY MINERALS SOCIETY REFERENCE CLAYS, *Clays Clay Miner.*, 50(3), 388–400, 2002.
- 922 Von Damm, K. L.: Seafloor Hydrothermal Activity: Black Smoker Chemistry And Chimneys, *Annu. Rev.*
923 *Earth Planet. Sci.*, 18(1), 173–204, doi:10.1146/annurev.earth.18.1.173, 1990.
- 924 Von Damm, K. L., Edmond, J. M., Measures, C. I. and Grant, B.: Chemistry of submarine hydrothermal
925 solutions at Guaymas Basin, Gulf of California, *Geochim. Cosmochim. Acta*, 49(11), 2221–2237, 1985.
- 926 Wallmann, K., Aloisi, G., Haeckel, M., Tishchenko, P., Pavlova, G., Greinert, J., Kutterolf, S. and
927 Eisenhauer, A.: Silicate weathering in anoxic marine sediments, *Geochim. Cosmochim. Acta*, 72(12),
928 2895–2918, doi:10.1016/j.gca.2008.03.026, 2008.
- 929 Zambardi, T. and Poitrasson, F.: Precise Determination of Silicon Isotopes in Silicate Rock Reference
930 Materials by MC-ICP-MS, *Geostand. Geoanalytical Res.*, 35(1), 89–99, doi:10.1111/j.1751-
931 908X.2010.00067.x, 2011.
- 932 Zheng, X., Beard, B. L., Reddy, T. R., Roden, E. E. and Johnson, C. M.: Abiologic silicon isotope
933 fractionation between aqueous Si and Fe (III) -Si gel in simulated Archean seawater : Implications for
934 Si isotope records in Precambrian sedimentary rocks, *Geochemica Cosmochim. Acta*, 187, 102–122,
935 2016.
- 936 Ziegler, K., Chadwick, O., Brzezinski, M. and Kelly, E. F.: Natural variations of $\delta^{30}\text{Si}$ ratios during
937 progressive basalt weathering, Hawaiian Islands, *Geochim. Cosmochim. Acta*, 69(19), 4597–4610,
938 doi:10.1016/j.gca.2005.05.008, 2005.
- 939
- 940



941

942 Tables

943

944 Table 1: Pore fluid Si concentration (μM), $\delta^{30}\text{Si}_{\text{pf}}$ values (‰) as well as biogenic silica weight fraction
945 (bSiO_2 in wt%), Al/Si ratio (mM/M), $\delta^{30}\text{Si}_{\text{bSiO}_2}$ values (‰), porosity (\emptyset), Al and K contents (wt%) for the
946 basin sites, hydrothermal site, and OMZ site.

947

948 Table 2: Water column and hydrothermal plume Si concentration (μM) and Si isotope values (‰).

949 Additionally, the share of hydrothermal fluids within the hydrothermal plume is given based on the
950 calculation provided by Berndt et al. (2016) in their supplementary materials.

951

952 Figures

953

954 Fig. 1. A) Location map of the sampling stations in the Guaymas Basin, Gulf of California. Black square
955 in the overview map indicates the sampling area. B) Sedimentary bSiO_2 content at each sampling
956 station. Water column stations were above MUC15-02 (VCTD02) in the basin, the hydrothermal site
957 (VCTD06, 09), and at the OMZ site (VCTD07).

958

959 Fig 2: Depth (cmbsf) profiles for all stations for pore fluid Si concentration (Si(OH)_4) in μM (grey
960 symbols) and $\delta^{30}\text{Si}_{\text{pf}}$ values (colored symbols) and biogenic opal weight fraction (bSiO_2) in wt% (grey
961 symbols) and $\delta^{30}\text{Si}_{\text{bSiO}_2}$ values (colored symbols). The dashed line is the $\delta^{30}\text{Si}$ value of the deep basin
962 (VCTD02) and the dotted line represents the $\delta^{30}\text{Si}$ value of the water column in the OMZ (VCTD07).
963 The uppermost Si isotope data point in the pore fluid diagrams refers to the bottom water (labelled
964 BW). Note the different depth scale for the OMZ site. The brackets around the MUC22-04 bottom
965 water Si concentration value indicate possible surface water contamination. Error bars not indicated
966 are within symbol size. The long-term error (2SD) of international standards is indicated in the upper
967 right $\delta^{30}\text{Si}_{\text{pf}}$ -depth profile.

968

969 Fig. 3. Pore fluid $\delta^{30}\text{Si}$ values are displayed versus the inverse Si concentration ($1/\text{Si}$) for the basin
970 sites, the hydrothermal site, and the OMZ site. Error bars not indicated are within symbol size. Mixing
971 curves are calculated after Eq. (3) between the respective water column and the average bSiO_2 $\delta^{30}\text{Si}$
972 value for all sites (see text for details).

973

974 Fig. 4. Asymptotic Si concentration (a) and the pore fluid $\delta^{30}\text{Si}_{\text{pf}}$ values (b) as a function of the
975 terrigenous/ bSiO_2 ratio for the basin sites, the hydrothermal site, and the OMZ site in the Guaymas



976 Basin. An exponential increase in silicate concentrations with decreasing terrigenous/bSiO₂ ratio is
977 observed, which is not reflected by corresponding systematic changes in $\delta^{30}\text{Si}_{\text{pf}}$. The values for the
978 terrigenous/bSiO₂ ratio defining the global trend (grey dots) are from the Southern Ocean, Scotia
979 Sea, Norwegian Sea, NE Atlantic, Juan de Fuca Ridge, Arabian Sea, and the Peru Basin (Van Cappellen
980 and Qiu, 1997a; Rabouille et al., 1997; Rickert, 2000).

981

982 Fig. 5. Conceptual model of the processes influencing pore fluid $\delta^{30}\text{Si}_{\text{pf}}$ values in the Guaymas Basin
983 (a) and the Peruvian margin (b). Bold values in the sediment show the average pore fluid $\delta^{30}\text{Si}_{\text{pf}}$
984 values. Arrow length indicates the dominating process (dissolution versus precipitation). The $\delta^{30}\text{Si}$
985 values in the hydrothermal plume indicate dilution with seawater (see section 4.5). (c) The average
986 pore fluid $\delta^{30}\text{Si}_{\text{pf}}$ values are shown, indicating the dominance of precipitation or dissolution processes
987 for the three settings in the Guaymas Basin and the Peruvian OMZ.

988

989 Fig. 6. Data and model results for OMZ core. a: Porosity. b: Biogenic opal concentration in solid
990 phase. c: K/Al ratio in solid phase. d: Dissolved silica concentration in pore fluids. e: Dissolved
991 potassium in pore fluids. f: Isotopic composition of dissolved silica. g: rate of biogenic opal
992 dissolution. h: Rate of authigenic phase precipitation. i: Rate of terrigenous phase dissolution.



Table 1

Station/MUC#/ Station name	Latitude (N) / Longitude (W)	Water depth (m)	Sediment																		
			Pore fluid					Sediment													
			Depth (cmbsf)	Si (μM)	$\delta^{30}\text{Si}$ pf (‰)	2SD (‰)	bSiO ₂ (wt%)	(Al/Si) bSiO ₂ (mM/M)	$\delta^{30}\text{Si}$ bSiO ₂ (‰)	2SD (‰)	Φ	Al mg g ⁻¹	K* mg g ⁻¹								
SO241-33/11/ Basin site	27° 33.301' 111° 32.883'	1855	BW	173	1.9	0.2	-	-	-	-	-	-	-	-	-	-	-	-	-	-	-
			0.5	381	1.3	0.2	22.6	39	0.8	0.1	0.932	44.4	13.7								
			1.5	455	-	-	23.1	-	-	-	0.920	45.2	13.9								
			2.5	563	1.2	0.1	24.2	-	-	-	0.905	46.3	14.1								
			3.5	635	-	-	22.4	-	-	-	0.894	-	-								
			4.5	685	-	-	-	-	-	-	0.892	49.1	14.7								
			6	686	-	-	25.2	-	-	-	0.875	39.2	12.4								
			8	745	-	-	-	-	-	-	0.857	-	-								
			10	726	-	-	21.9	-	-	-	0.852	-	-								
			12.5	737	0.9	0.2	18.5	-	-	-	0.826	53.2	16.0								
15.5	750	-	-	14.4	-	-	-	0.800	61.4	17.9											
18.5	751	-	-	14.8	-	-	-	0.787	-	-											
22	712	1.2	0.2	19.6	26	0.8	0.2	0.801	59.5	17.5											
SO241-22/04/ Basin site	27° 28.165' 111° 28.347'	1839	BW	54	2.0	0.2	-	-	-	-	-	-	-	-	-	-	-	-	-	-	-
			0.5	349	1.0	0.2	11.6	37	0.9	0.2	0.910	57.8	17.0								
			1.5	377	-	-	-	-	-	-	0.907	-	-								
			2.5	394	-	-	-	-	-	-	0.890	53.6	16.4								
			3.5	421	-	-	-	-	-	0.897	-	-									
			4.5	474	-	-	-	-	-	0.895	-	-									
			5.5	558	1.1	0.1	10.9	-	-	-	0.893	58.7	17.3								
			7	590	-	-	-	-	-	-	0.895	-	-								
			9	637	1.2	0.2	13.1	-	-	-	0.890	58.6	17.2								
			11	636	-	-	-	-	-	-	0.891	-	-								
13	597	-	-	-	-	-	-	0.895	-	-											
15.5	545	-	-	-	-	-	-	0.896	-	-											
18.5	440	1.5	0.2	7.6	-	-	-	0.895	57.9	17.3											
22	404	-	-	-	-	-	-	0.876	-	-											
26	364	1.3	0.2	9.8	71	0.5	0.2	0.842	66.6	19.4											



2.5	702	-	-	-	-	-	-	-	0.855	17.4	4.4
3.5	752	-	-	-	-	-	-	-	0.820	16.7	4.1
4.5	781	-	-	-	-	-	-	-	0.808	16.0	3.8
5.5	781	2.2	0.1	11.0	-	-	-	-	0.793	15.4	3.5
6.5	875	-	-	-	-	-	-	-	0.775	14.8	3.3
9	877	-	-	-	-	-	-	-	0.770	13.4	2.7
11	892	-	-	7.0	-	-	-	-	0.742	9.4	1.3
13	914	-	-	4.7	-	-	-	-	0.810	17.8	3.9
15.5	903	-	-	14.6	-	-	-	-	0.802	21.9	5.4
18.5	888	1.8	0.1	8.2	35	0.9	0.1	0.620	2.9	-	-
BW	31	0.8	0.2	-	-	-	-	-	-	-	-
0.5	247	-0.5	0.3	15.3	-	-	-	0.970	35.1	12.67	-
1.5	425	-	-	-	-	-	-	0.954	46.6	14.0	-
2.5	458	-0.3	0.1	16.9	-	-	-	0.945	48.9	14.9	-
3.5	492	-	-	-	-	-	-	0.947	47.2	14.7	-
4.5	569	-	-	-	-	-	-	0.939	48.6	15.0	-
5.5	618	0.3	0.2	15.3	-	-	-	0.935	51.1	15.3	-
6.5	655	-	-	-	-	-	-	0.928	50.4	15.4	-
7.5	735	-	-	-	-	-	-	0.923	53.4	16.2	-
9	763	0.0	0.2	13.5	-	-	-	0.926	51.8	15.8	-
11	754	-	-	-	-	-	-	0.926	39.5	10.1	-
13	753	-	-	-	-	-	-	0.929	48.6	14.2	-
15	767	-	-	16.23	26	0.8	0.1	0.909	53.3	15.9	-
18.5	772	-	-	-	-	-	-	0.913	53.8	15.9	-
20.5	781	-0.2	0.2	18.1	-	-	-	0.911	53.3	15.7	-
23.5	763	-	-	-	-	-	-	0.906	56.1	16.8	-
26.5	765	-	-	-	-	-	-	0.919	47.8	14.5	-
29	763	-	-	-	-	-	-	0.929	41.5	12.6	-
30	768	-	-	-	-	-	-	0.925	45.9	13.9	-
38	760	0.8	0.2	21.9	-	-	-	0.925	45.8	13.5	-

Φ = porosity
 * porosity corrected



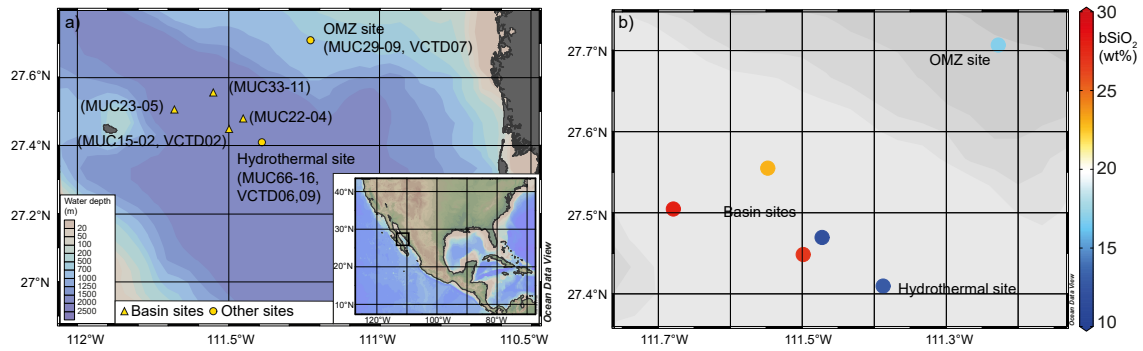
Table 2

Cruise-Station/VCTD#/ bottle#/Station name	Latitude (N) / Longitude (W)	Depth	Si	$\delta^{30}\text{Si}$	2SD	hydrothermal fluid share*
		(mbsl)	(μM)	(‰)	(‰)	(%)
Water column						
SO241-12/02/ Basin site	27° 26.133 111° 30.268	1844	163	1.5	0.1	0.1
SO241-42/07/ OMZ site	27° 42.411 111° 13.663	586	78	1.5	0.2	0
Hydrothermal plume						
SO241-67/09/06/ Hydrothermal site	27° 24.750 111° 23.240	1800	253	0.7	0.1	2.1
SO241-67/09/09/ Hydrothermal site	27° 24.750 111° 23.240	1800	206	1.4	0.2	0.2
SO241-67/09/12/ Hydrothermal site	27° 24.750 111° 23.240	1800	690	1.0	0.2	5.7

* calculation in Berndt et al. (2016)



Fig. 1



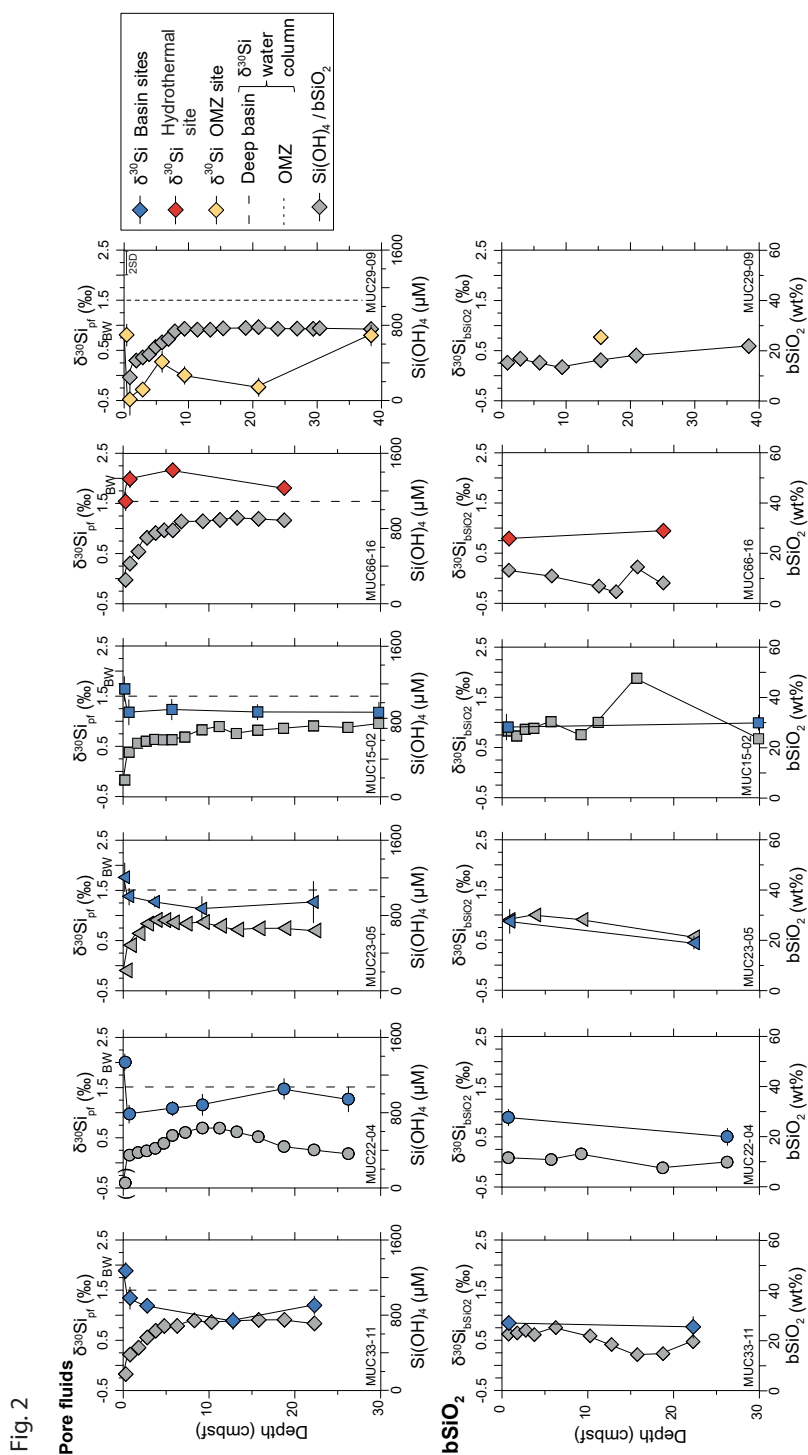




Fig. 3

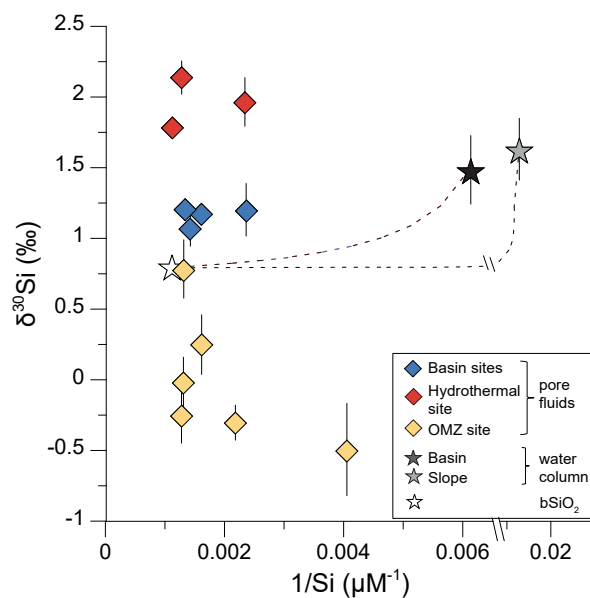




Fig. 4

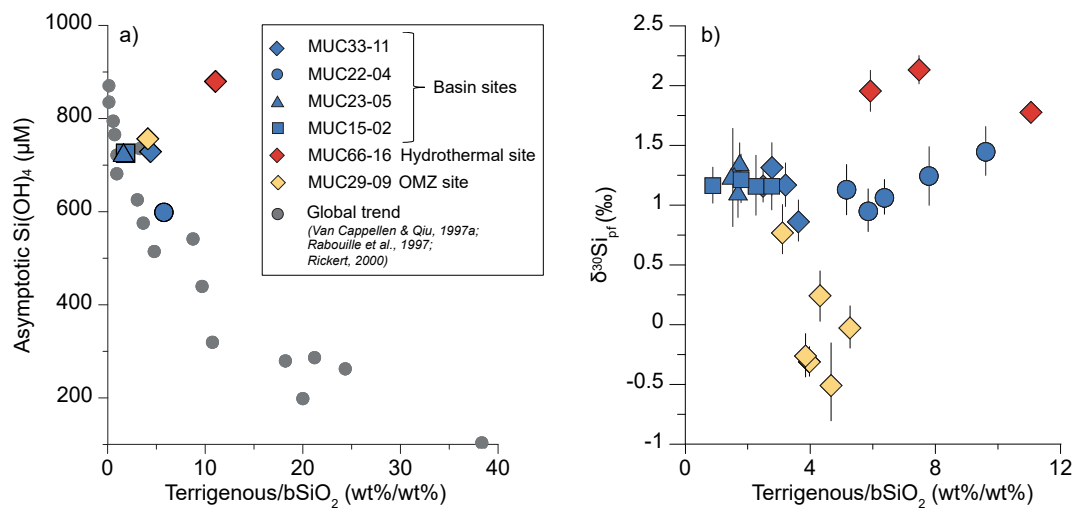




Fig. 5

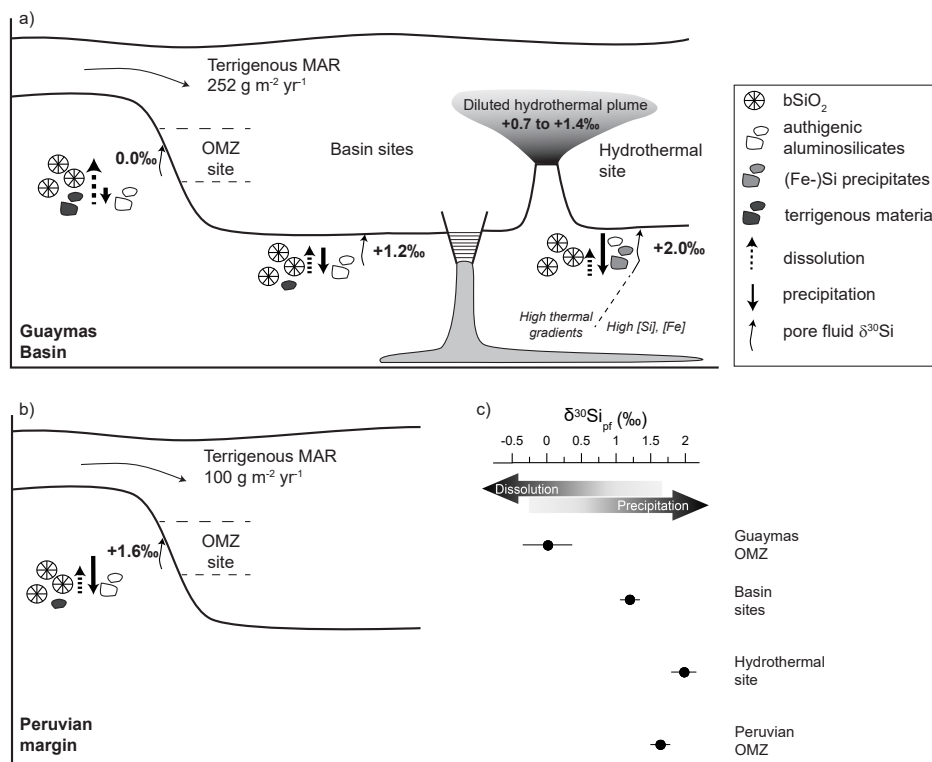




Fig. 6

